

RESEARCH ARTICLE

NEUROSCIENCE

Dynamic compartmental computations in tuft dendrites of layer 5 neurons during motor behavior

Yara Otor^{1†}, Shay Achvat^{1†}, Nathan Cermak¹, Hadas Benisty², Maisan Abboud¹, Omri Barak¹, Yitzhak Schiller¹, Alon Poleg-Polsky^{3*}, Jackie Schiller^{1*}

Tuft dendrites of layer 5 pyramidal neurons form specialized compartments important for motor learning and performance, yet their computational capabilities remain unclear. Structural-functional mapping of the tuft tree from the motor cortex during motor tasks revealed two morphologically distinct populations of layer 5 pyramidal tract neurons (PTNs) that exhibit specific tuft computational properties. Early bifurcating and large nexus PTNs showed marked tuft functional compartmentalization, representing different motor variable combinations within and between their two tuft hemi-trees. By contrast, late bifurcating and smaller nexus PTNs showed synchronous tuft activation. Dendritic structure and dynamic recruitment of the *N*-methyl-D-aspartate (NMDA)-spiking mechanism explained the differential compartmentalization patterns. Our findings support a morphologically dependent framework for motor computations, in which independent amplification units can be combinatorially recruited to represent different motor sequences within the same tree.

Cortical pyramidal neurons (PNs) typically possess an elaborate dendritic tree, which serves to receive and integrate the vast synaptic inputs arriving to the neuron. In vitro and modeling studies have established the role of passive, active, and morphological properties of the dendritic tree in information processing. Especially important are local dendritic *N*-methyl-D-aspartate (NMDA) and calcium spikes, which endow PNs with the capability of performing multicompartmental parallel nonlinear computations, potentially increasing the computational power and storage capacity of PNs and ultimately of the network (1–5).

In vivo evidence for local representation of information in different tuft dendrites of layer 5 PNs is scarce (6, 7). Most reports show that the vast majority of calcium signals are highly correlated between different tuft branches, apical dendrites, and soma of same neurons (8–13), suggesting that the tuft and apical branches function mostly as a single compartment (14, 15). Thus, current literature presents a puzzling gap between the powerful computational capabilities of these dendrites, as suggested by in vitro and modeling studies (1, 16–22), and the much simpler computational scheme emerging from in vivo experiments.

In most in vivo studies, little consideration is given to the anatomical apical tuft structure

of the layer 5 PNs. Layer 5 PNs are composed of two main anatomical subtypes that differ in their dendritic apical morphology: thick-tufted pyramidal tract (PT) and slender-tufted intra-telencephalic (IT) neurons (23–30). Thick-tufted PTNs are further subdivided into two distinct subtypes on the basis of their nexus morphology and molecular markers (23, 24, 26, 31, 32). Because the degree of compartmentalization and electrical coupling is strongly dependent on the dendritic morphology (19, 33), we set out to examine motor representation in tuft dendrites of these two morphological types of thick-tufted layer 5 PTNs (24, 26) in the primary motor cortex (M1) (28–30). We developed a comprehensive experimental and analysis platform to reveal the relationships between the detailed structural pattern and the behaviorally related calcium activity.

Results

We imaged the activity of tuft dendrites from single thick-tufted layer 5 PTNs in M1 forelimb cortex using two-photon calcium imaging during two head-fixed behavioral paradigms: a hand reach and grab for a food pellet (34) and running on treadmill tasks (35) (Fig. 1, A and B). We used the sparse labeling method of adeno-associated virus (AAV) viral vectors encoding two fluorescent proteins: GCaMP6 for recording the activity (36) and mRuby2 for reconstructing the morphology of the tree (Fig. 1, C to F) with a high degree of certainty. This resulted in the transfection of only a few layer 5 PTNs in our field of view (Fig. 1E; see materials and methods) and enabled us to trace tuft dendrites to their parent soma with high accuracy. Overall, we recorded 28 thick-

tufted layer 5 PTNs in 22 mice. We first reconstructed the dendritic morphology from the two-photon volumetric Z-stack (Fig. 1C). We then used single-plane calcium imaging (30-Hz frame rate) to simultaneously record the activity of multiple dendritic tuft regions of interest (ROIs) of the same neuron (Fig. 1, E and F; on average, for each tree we sampled from $80.4 \pm 11\%$ of the terminal branches). These ROIs were aligned to the anatomical tree structure using custom software (see materials and methods).

Thick-tufted layer 5 PTNs are divided into two main well-established subtypes on the basis of their apical dendritic morphology with early and late bifurcating apical trunk (24, 26, 27). We used hierarchical clustering to subdivide our thick-tufted layer 5 PTNs on the basis of five morphological features (Fig. 1G and fig. S1, A to E). Consistent with previous studies, the clustering yielded two main subclasses: type 1, with early bifurcating apical tuft and long nexus, and type 2, with late bifurcating apical tuft and shorter nexus (Fig. 1G and fig. S1, F to H). Retrograde viral tracing of PTNs projecting to the medulla or cervical spinal cord revealed that M1 corticospinal PTNs yield a high proportion of type 1 dendritic morphology (fig. S1, I and J; 10 out of 11 of neurons in four mice were classified as type 1 neurons).

The two PTN subtypes demonstrated clear differences in their tuft calcium signals recorded during motor task performance. This was already apparent in the raw calcium imaging traces of individual trials (Fig. 1H, fig. S2, and movies S1 to S6). Type 1 thick-tufted layer 5 PTNs showed pronounced independent activity across their dendritic tuft branches (Fig. 1H and fig. S2), both in branches belonging to their right or left (R/L) tuft hemi-trees (Fig. 1H and fig. S2; division to left and right hemi-trees defined as all descendants of the first bifurcation branches) and within the hemi-trees (Fig. 1H). By contrast, type 2 PTNs did not show hemi-tree compartmentalization but did show more uniform dendritic tuft activation across their entire tuft tree (Fig. 1H and fig. S2).

To quantitatively investigate the correlations between the detailed tuft tree structure and dendritic activity in type 1 and 2 PTNs, we constructed and compared ROI distance matrices on the basis of dendritic structure and calcium activity. We obtained a structural distance matrix of the tuft tree by measuring the shortest path distance between all pairwise combinations of ROI locations, organized according to the tree structure (Fig. 1I). Calcium activity was extracted by identifying the calcium events in each ROI for all trials with the modified event detector MLSPIKE (37) (materials and methods and fig. S3A).

Calcium event amplitudes exhibited a long-tailed asymmetrical distribution (Fig. 1J and

¹Department of Physiology, Technion Medical School, Bat-Galim, Haifa 31096, Israel. ²Yale University School of Medicine; Bethany, CT, USA. ³Department of Physiology and Biophysics; University of Colorado School of Medicine, 12800 East 19th Avenue MS8307, Aurora, CO 8004, USA.

*Corresponding author. Email: jackie@technion.ac.il (J.S.); alon.poleg-polsky@cuanschutz.edu (A.P.-P.)

†These authors contributed equally to this work.

Fig. 1. M1 contains two populations of thick-tufted layer-5 PTNs with distinct morphologies and functional properties. (A) (Top) Behavioral setup for hand reach task. (Bottom) An ethogram and histogram annotating the behavior of an expert mouse.

(B) (Top) Behavioral setup of head-fixed mice running on a treadmill. (Bottom) Example of velocity (cm/s) over time (s). (C and D) Z-stack of a single PTN acquired in vivo and its three-dimensional anatomical reconstruction.

(E) Single-imaging plane of a GCaMP6s-positive layer 5 PTN's tuft dendrites. ROIs are marked in yellow. (F) Schematics of the tuft morphology; dots represent ROIs. Same neuron in (C) to (F). (G) (Top) Hierarchical clustering of thick-tufted layer 5 PTNs based on five morphological parameters. (Bottom) Three example apical morphologies from each PTN type. Basal and oblique dendrites are not shown. Red numbers indicate the corresponding neurons in the clustering.

(H) Calcium events ($\Delta F/F$ heat map) in single trials from the same three type 1 (left) and type 2 (right) PTNs shown in (G), arranged by the tree structure as indicated by the dendrogram. (I) Illustration of structure-activity correlations. Schematic representation of a layer 5 PTN with structural distance matrix presented as a heat map of the shortest path distance between each two ROIs (left) and illustrated activity traces for ROIs (right upper panel, dashed rectangles mark events belonging to different event clusters) and activity matrix showing Pearson correlation between ROI pairs presented for all events and for each event cluster (right lower panel).

(J) (Left) Normalized calcium events histogram from 21 neurons for type 1 (black) and type 2 (gray) PTNs. (Right) Event distribution color coded by event cluster type for individual sessions in multiple neurons.

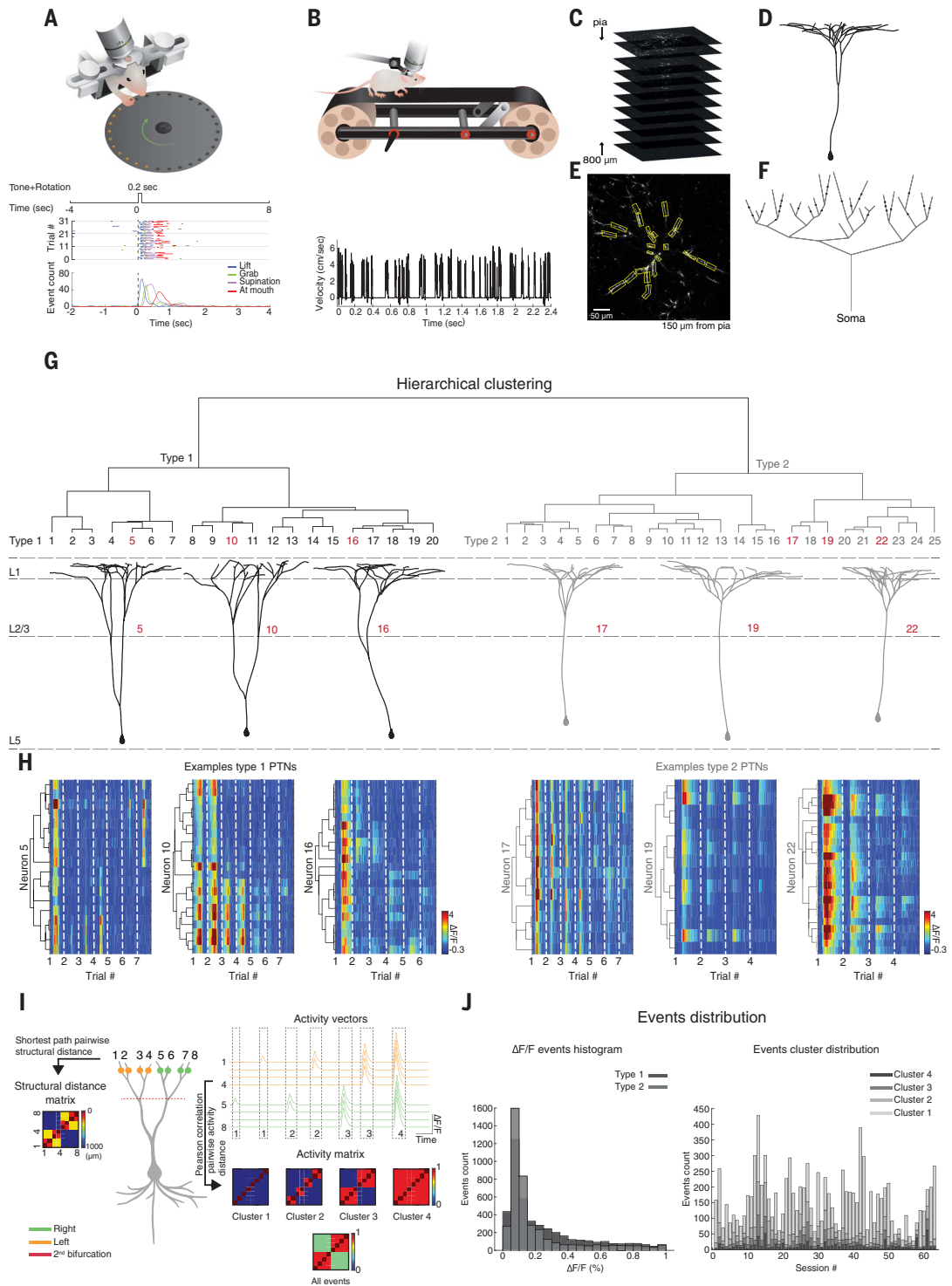


Fig. 2A). This raised the possibility of multiple subpopulations of calcium events. Indeed, visual inspection suggested four qualitatively distinct types of activation patterns in type 1 PTNs (single branch, subtree, hemi-tree, whole tree; Fig. 1, H and I; Fig. 2B; and fig. S2). To perform quantitative analysis of these differ-

ent event types, we subdivided the events into four clusters according to either their average amplitudes over all ROIs (see materials and methods) or the number of activated ROIs during each event (spatial activation extent) using the k-means algorithm (average percentage of events in cluster 1 = 66%, cluster 2 =

17%, cluster 3 = 10%, cluster 4 = 8% of the events; Fig. 1H, Fig. 2B, and figs. S2 and S3). With the calcium activity vectors and the structural distance matrix at hand, we constructed a pairwise Pearson correlation activity matrix arranged according to the structural distance matrix for each of the

Fig. 2. Compartmentalized activity in tuft dendrites of type 1 thick-tufted layer 5 PTNs during running on treadmill and hand reach.

(A) Calcium events histogram from one type 1 PTN during treadmill session. Arrows indicate values separating the four different event clusters.

(B) Examples of calcium events ($\Delta F/F$ heatmap) from the four event clusters in type 1 PTN. ROIs are arranged by the tree structure as indicated by the dendrogram, shown on the left (R, green; L, orange). (C) Two-dimensional tree diagram (left) and the corresponding structural distance matrix and dendrogram (right) of a type 1 PTN. Dots represent recorded ROIs.

(D) Two-dimensional PCA embedding of all ROIs activity; each dot represents a single ROI. (E) (Top) Matrices showing pairwise Pearson correlation coefficients computed from the calcium signals arranged by the tree structure shown in (C). (Bottom) Pearson correlation values as a function of shortest path distance fitted with a linear regression model. [(A) to (E)] Same neuron and session. ROIs compared within left hemi-tree (orange); within right hemi-tree (green) and between R/L hemi-trees (red). Black line represents linear regression model fit.

(F to H) As in (C) to (E) for a different type 1 PTN during a hand reach session. (I to M) Box plots of the following parameters: Mantel statistics comparing Pearson correlation and structural distance matrices (I), R^2 of linear regression model that predicted Pearson correlations

by distance (J), slope of linear regression model that predicted Pearson correlations by distance (K), R^2 of linear regression model that predicted Pearson correlations by distance calculated for the hemi-trees separately (L), and Z-score of the experimental Pearson correlations of within compared to between hemi-trees (mean $\text{Pearson}_{\text{within}} - \text{mean Pearson}_{\text{between}}$) calculated in relation to the shuffled distribution (M). * $p < 0.05$, ** $p < 0.01$, *** $p < 0.001$; blue asterisk, mean value. One-way analysis of variance (ANOVA) with Tukey post-hoc test (12 neurons, 8 animals, 27 sessions).

four calcium event clusters and for all events (Fig. 1, I and J).

We quantified the anatomical-functional correlations using three measures: First, we

performed principal component analysis (PCA) to embed the activity of each ROI across time and trials into a two-dimensional space of the two leading components that explain $84.42 \pm$

9.67% of the variance. Second, we used a Mantel test (38–40), which quantifies the degree of correlation between the functional activity and structural distance matrices. Third, we

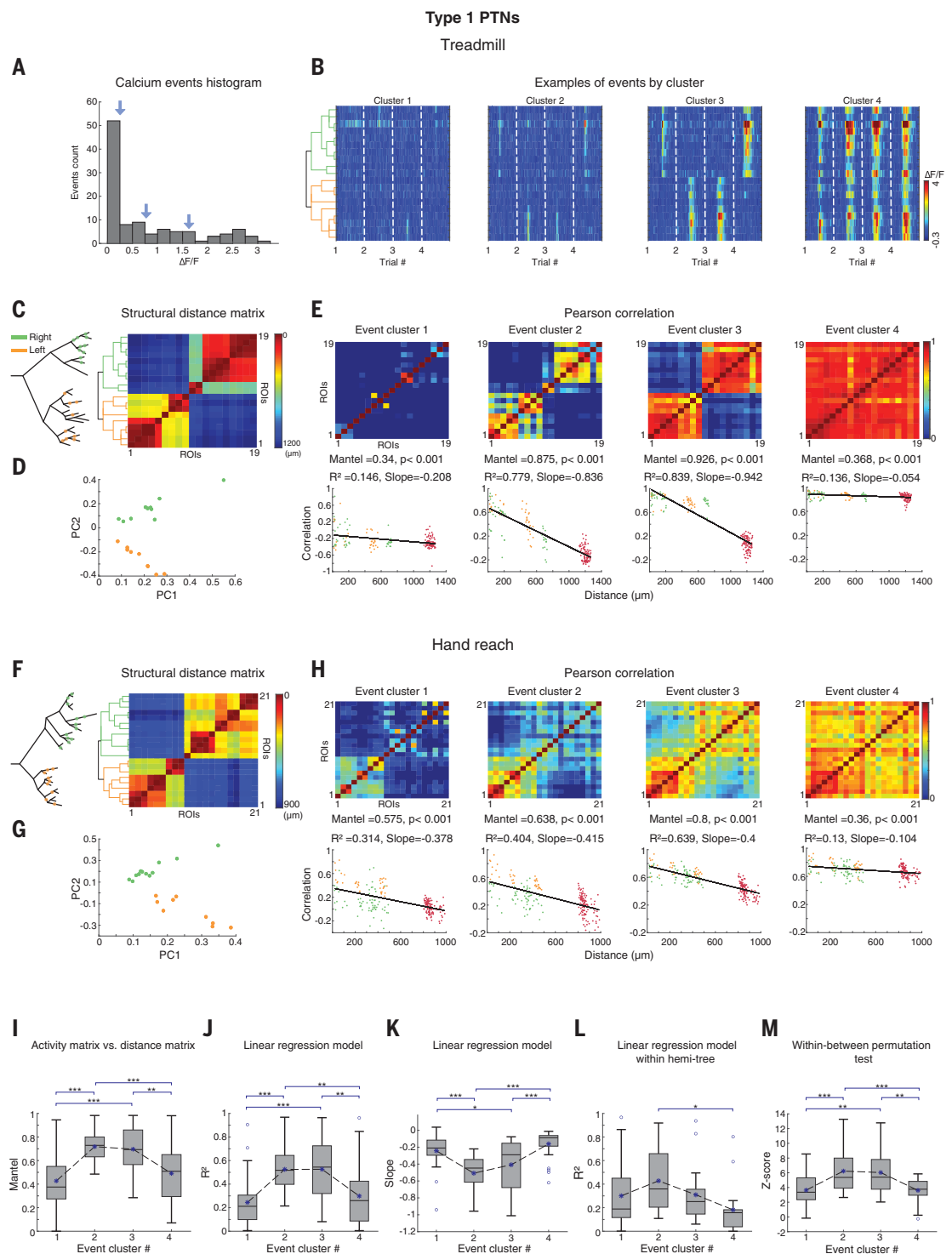
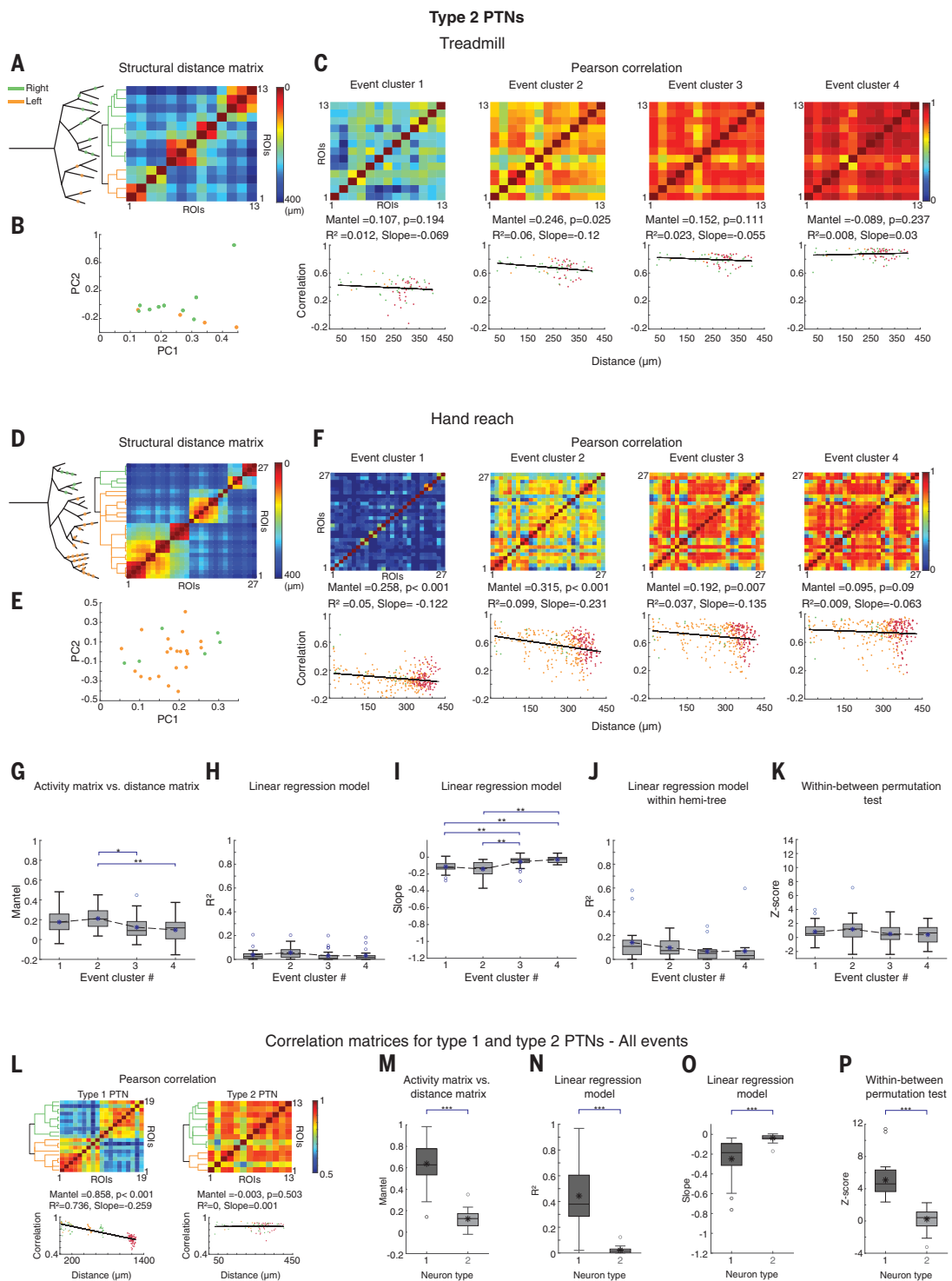


Fig. 3. Homogeneous activity in tuft dendrites of type 2 thick-tufted layer 5 PTNs during running on treadmill and hand reach.

(A to K) As in (C) to (M) of Fig. 2 for type 2 PTNs. * $p < 0.05$, ** $p < 0.01$, *** $p < 0.001$; blue asterisk, mean value. One-way ANOVA with Tukey post-hoc test (9 neurons, 9 animals, 25 sessions). (L) Pairwise Pearson correlation coefficient matrices computed for all calcium events for type 1 (left) and type 2 (right) PTNs. (Bottom) Pearson correlation values as a function of shortest path distance fitted with a linear regression model for all events calculated for type 1 (left) and type 2 (right) PTNs. Type 1 PTN as in Fig. 2, C to E, and type 2 as in (A) to (C). (M to P) Box plots are the same as in (G) to (I) and (K) when all calcium events are considered for type 1 and type 2 PTNs.



measured the relationship between the pairwise Pearson activity correlations to the distance between ROIs with a linear regression (Fig. 2, C to H).

We first concentrated on type 1 PTNs. We observed strong compartmentalization of the tuft tree with a significant correlation between the tree structure and calcium activity during both motor tasks: hand reach and running on

treadmill. The first cluster, with the smallest calcium event amplitudes, typically involved correlated activity of individual or sister branches (Fig. 2, E and H). For this cluster, the Mantel statistics were relatively low (Fig. 2I), as was the linear correlation between the Pearson values and dendritic distance (Fig. 2, J to L, and fig. S4A; linear regression permutation test). For events with intermediate am-

plitudes corresponding to clusters 2 and 3, we observed high correlation between the activity and the tree structure, with strong compartmentalization of the tuft tree, ranging from correlated activity mapped to secondary and tertiary branches (event cluster 2; Fig. 2, C to H) or entire hemi-trees (event cluster 3; Fig. 2, C to H). The strong correlation between the anatomical and activity matrices in these

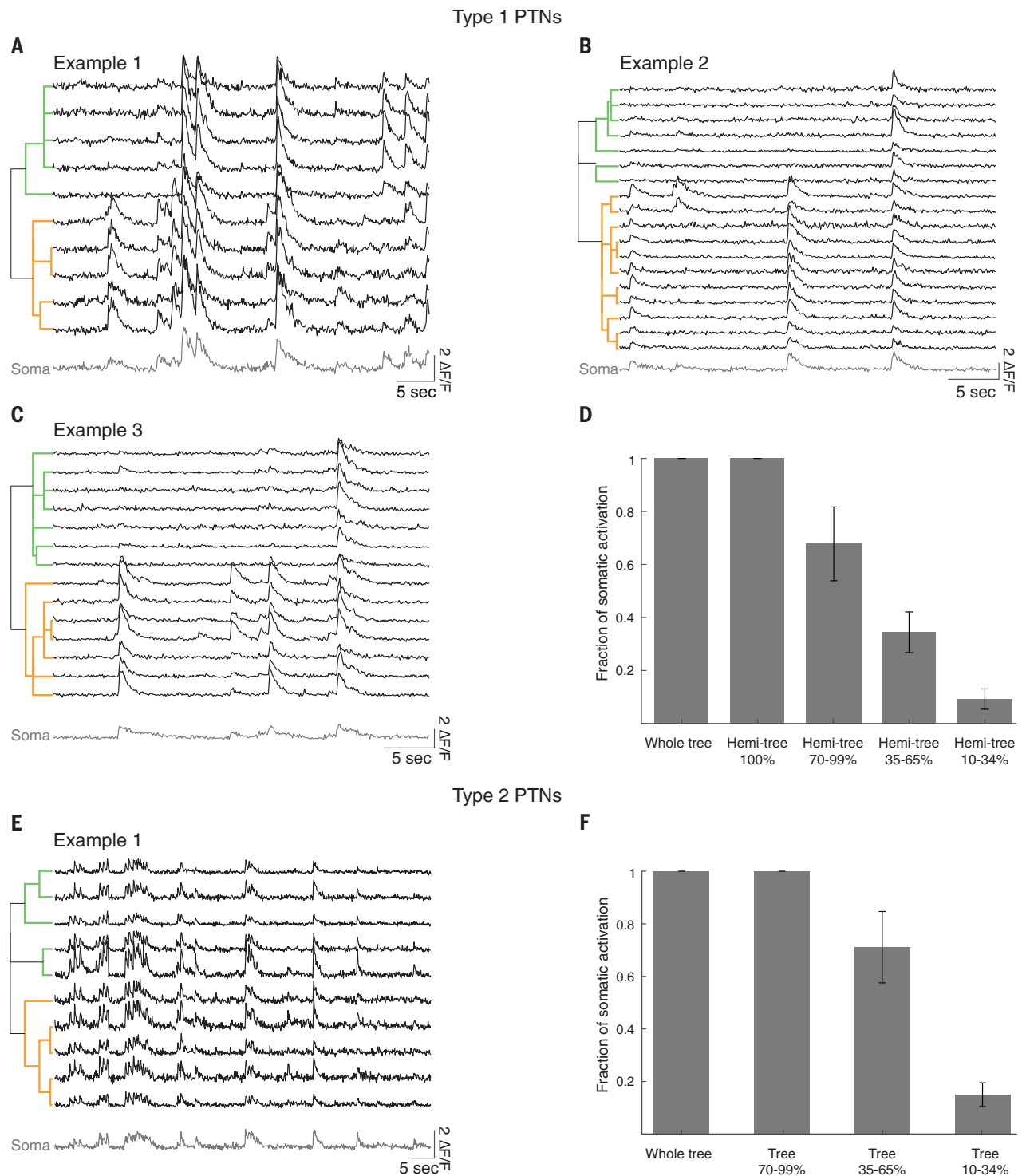


Fig. 4. Tuft and soma activity correlations. Quasi-simultaneous tuft and soma recordings were performed with an electrically tunable lens (ETL) (~10 Hz) in type 1 and 2 PTNs. **(A to C)** Examples of representative $\Delta F/F$ traces in the tuft and soma from a type 1 PTN (ROIs are arranged by the tree structure as indicated

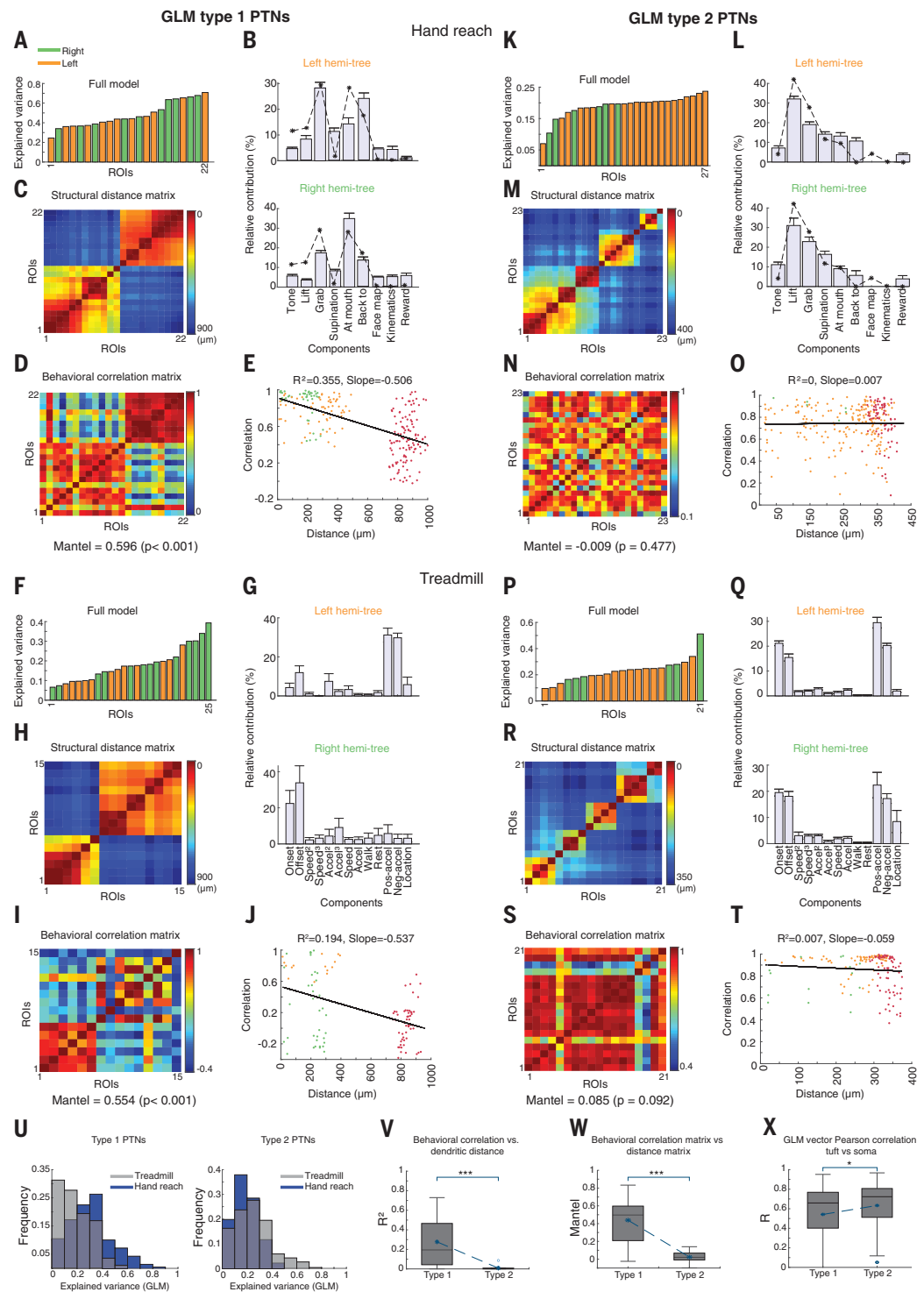
by the dendrogram). **(D)** Mean (\pm SD) fraction of tuft events that were simultaneously active with the soma for type 1 PTNs (seven neurons, six animals). **(E)** As in **(A)** for a type 2 PTN. **(F)** As in **(D)** for type 2 PTNs (three neurons, three animals).

clusters resulted in higher Mantel statistics (Fig. 2I) and a stronger dependence between pairwise Pearson correlations and tuft dendritic distance (Fig. 2, E, H, and J to L, and fig. S4A; linear regression permutation test).

Finally, for the largest-amplitude calcium events (cluster 4), the activity was spread throughout the entire tuft tree, and responses in all ROIs were highly correlated (Fig. 2, E and H). This was manifested as lower Mantel

statistics (Fig. 2I) and lower dependence of the pairwise Pearson correlation values on dendritic distance (Fig. 2, E, H, and J to L, and fig. S4A; linear regression permutation test). Even in cluster 4 events, it is evident that some

Fig. 5. Modeling the contribution of the behavioral predictors to calcium activity of type 1 and type 2 PTNs using a generalized linear model (GLM). (A) Goodness of fit (R^2) of GLM full model for each ROI from a type 1 PTN during a hand reach session. (B) Mean relative contribution of modeled ROIs ($R^2 > 15\%$) for each of the behavioral predictors for right and left hemi-trees. Black asterisks on both graphs indicate values computed from somatic recordings of same neuron. (C) Structural distance matrix. ROIs with $R^2 < 0.15$ were excluded. (D) Pairwise Pearson correlation between the GLM relative contribution vectors for all included ROI pairs, arranged by the tree structure. (E) Pearson correlation values shown in (D) as a function of shortest path distance fitted with a linear regression model. (F to J) As in (A) to (E) during running on a treadmill. Same neuron in (A) to (J). (K to T) As in (A) to (J) for an example type 2 PTN. (U) (Left) Frequency of ROI's R^2 values of GLM full model for type 1 PTNs (10 animals, 14 neurons, 31 sessions). (Right) As in left panel for type 2 PTNs (9 animals, 10 neurons, 31 sessions). (V to X) Box plots of the following parameters: R^2 linear regression model that predicted the Pearson correlations of GLM relative contribution vector by dendritic distance (V), Mantel statistics comparing the structural distance matrix and the behavioral-correlation matrix (W), Pearson correlation between the soma's behavioral relative contributions and those of the tuft, for type 1 and type 2 PTNs (seven and four neurons, respectively) (X). *** $p < 0.001$; blue asterisks, mean value. Wilcoxon rank test.



portions of the tree were more strongly correlated than others. Similar results were obtained when event clustering was based on the spatial extent of calcium signals instead of their averaged amplitude (fig. S5).

To further examine the R/L hemi-tree segregation, we used two additional analysis methods: First, we shuffled the “within” and “between” tagging of ROI Pearson correla-

tion pairs while maintaining their pairwise correlation coefficient values. We found the experimental values of the difference between the mean Pearson correlations of within compared to between hemi-trees to be significantly higher compared to the shuffled distribution for all cluster events (Fig. 2M and fig. S6, A and C; Z-score > 3.6). Second, we calculated the proportion of the variance explained (R^2) of

the calcium activity of each ROI in one hemi-tree by the activity of all ROIs in the contralateral hemi-tree using a linear regression model. The results further indicated compartmentalization of activity in the hemi-trees in clusters 1 to 3 (fig. S7A).

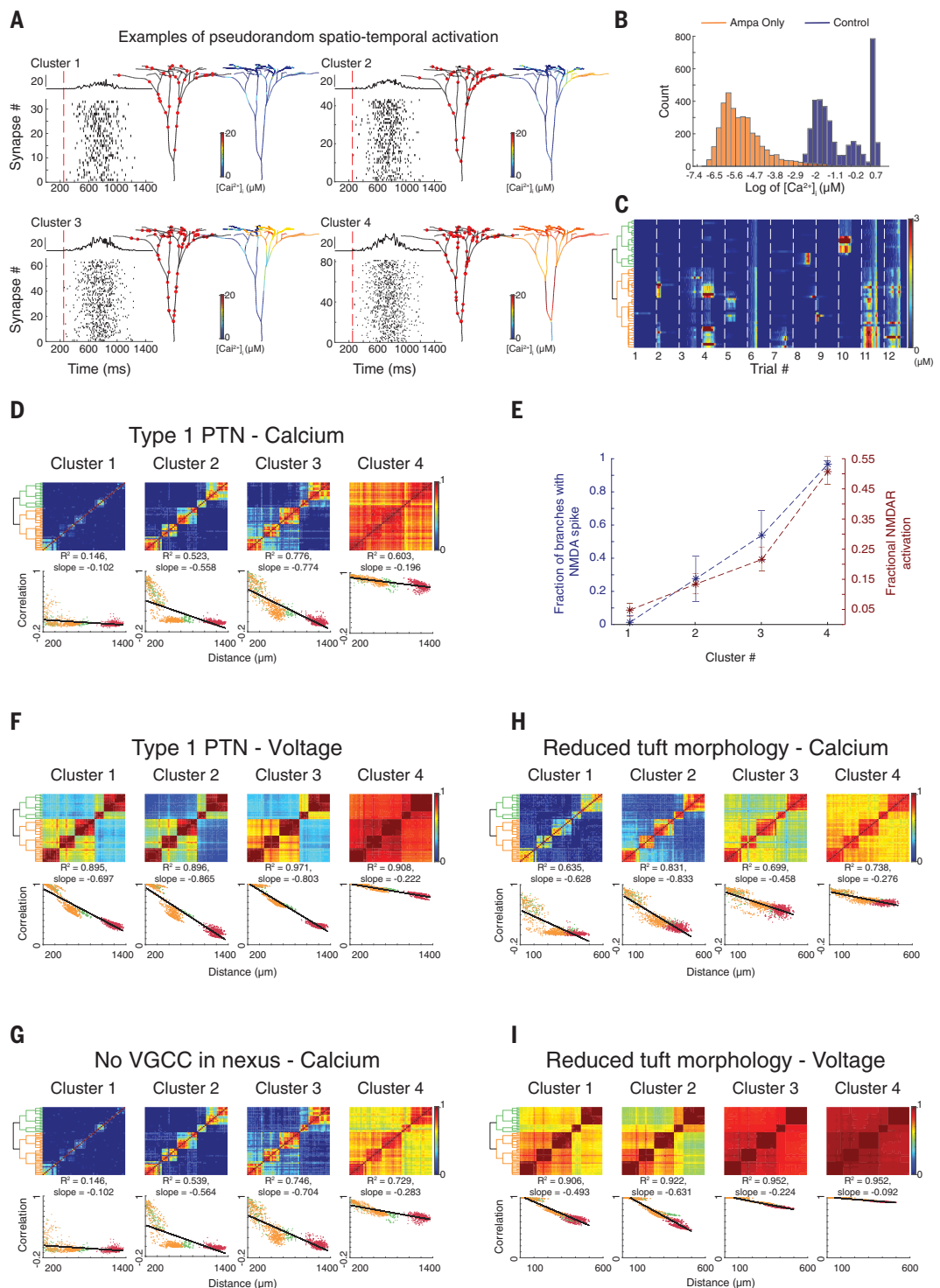
To facilitate the comparison between type 1 and type 2 PTNs, we also divided the events of type 2 PTNs into four clusters. The distributions

Fig. 6. Simulation of type 1 PTN explains in vivo activity by apical morphology and NMDA spikes.

(A) Examples of the temporal distribution of simulated pseudorandom synaptic activation patterns for the four event clusters in one trial. Top trace, the total number of activated synapses over time. (Right) The corresponding spatial input distribution and post-synaptic calcium signal (shown on a logarithmic scale). The average number of recruited synapses for each event cluster was 34 ± 13 , 48 ± 13 , 60 ± 15 , and 84 ± 29 .

(B) The distribution of the simulated evoked calcium events in the tuft dendrites of the reconstructed type 1 PTN. (C) Representative calcium activity in different simulation trials, arranged by the tree structure as indicated by the dendrogram. (D) (Top) Pairwise Pearson correlation coefficients computed from the tuft calcium signals arranged by the tree structure. (Bottom) Pearson correlation values as a function of shortest path distance fitted with a linear regression model (black).

(E) The normalized number of tuft dendrites with NMDA spikes (blue) and the fractional NMDAR conductance (brown) for all event clusters. Error bars: SD. (F) As in (D), for tuft voltage correlations. (G) As in (D), in the absence of VGCC in the nexus. (H) As in (D), when the morphology of the tuft was reduced to match the extent of the tuft dendrites in type 2 PTNs shown in fig. S13A. (I) As in (H), for tuft voltage correlations. Color coding: orange and green represent data from the left and right hemitrees, respectively. Red, comparison between R/L hemi-trees. Simulations for this figure are for the neuron in Fig. 2, C to E.



of peak calcium events and the peak calcium amplitudes of the clusters were comparable in type 1 and 2 PTNs (fig. S3, C and D). Type 2 PTNs did not show significant correlations between their tree structure and functional calcium activity for any of the calcium event clusters (Fig. 3 and figs. S4B and S7, B to E), and compartmentalization between their R/L hemi-tree was low (figs. S6, B and C, and S7A).

Thus, for type 2 PTNs except cluster 1, calcium events globally involved the entire tuft tree, consistent with previous reports in visual, anterior lateral motor (ALM), and somatosensory cortices (8–11). The differences in the structure-function correlations between type 1 and type 2 PTNs were not related to the cluster subdivision. They were also evident when the analysis was performed on the whole event population (Fig. 3,

L to P). However, in type 1 PTNs, the subdivision into the four clusters highlighted more details because using the entire population averaged events with different spatial activation patterns.

Plotting Mantel statistics as a function of nexus size for individual neurons, we found a clear distinction between the two PTN subclasses despite the variability in size within both groups Support Vector Machine (SVM) accuracy 1,

chance 0.52 for both clusters). This finding further strengthens the anatomical subdivision based on independent physiological parameters (fig. S7F).

We next investigated the relationship between tuft tree and somatic activation using quasi-simultaneous imaging of tuft and soma (~10-Hz acquisition rate). For type 1 PTNs, we observed that events encompassing the full tuft or restricted to an entire hemi-tree were invariably associated with somatic activation in all (100%) events examined. For events encompassing only part of a hemi-tree, somatic activation was proportional to the percentage of active ROIs (Fig. 4, A to D). In type 2 PTNs, somatic activation was proportional to the extent of ROI recruitment in the entire tree (Fig. 4, E and F). The tuft activity was critically dependent on NMDA receptor (NMDR) channels because local injection of the NMDAR blocker MK801 close to the imaged tuft blocked both tuft and somatic activity (fig. S8).

Next, we investigated the possible functional importance of tuft compartmentalization. For both type 1 and type 2 PTNs, the activity in tuft dendrites strongly correlated with motor behavior (fig. S9). To evaluate the preferential selectivity of responses for specific behavioral variables in the different tuft dendrites in individual neurons, we modeled the calcium transients using a generalized linear model (GLM) (Fig. 5 and fig. S10A; see materials and methods) (34, 41, 42). For both type 1 and type 2 layer 5 PTNs, the activity in tuft dendrites was strongly related to individual motor variables. The GLM effectively modeled the calcium activity of both hand reach and running on treadmill behavioral events (Fig. 5). On average, for type 1 and type 2 PTNs, the full GLM successfully modeled the ROIs activity, achieving explained variance >0.15 in 77.5 and 63.8% of ROIs for the hand reach task and 56.5 and 73% of ROIs for the treadmill task, respectively (Fig. 5U).

For type 1 PTNs, representation was not uniform throughout the tuft for either hand reach or treadmill behaviors. We observed a differential representation of motor variables in the different tuft tree segments (Fig. 5, A to J and V to W, and fig. S10B). The largest nonuniformity was typically observed between the R/L tuft hemi-trees with different combinations of motor variables preferentially encoded by each of the two hemi-trees activity (Fig. 5, A to J, and fig. S10B). However, we also could observe dendrites within each hemi-tree, which were tuned to different combinations of motor variables (fig. S10B). To quantify the spatial compartmentalization of motor variables representation within and between the hemi-trees of single type 1 PTNs, we performed pairwise Pearson correlations between the GLM selectivity vectors of the dif-

ferent ROIs (Fig. 5, D, E, I, and J, and fig. S10B). Overall, type 1 PTNs demonstrated a correlation between the pairwise Pearson correlation coefficient of the GLM selectivity vectors and the distance between ROIs (Fig. 5, A to J and V). Consistently, we observed a significant correlation between the tuft distance matrix and GLM vector matrix for both behavioral data (Fig. 5, V and W). The significance of R/L segregation was further examined by comparing our experimental Pearson correlations between R/L hemi-trees to randomly distributed ROIs (1000 permutations). Experimental Pearson values between R/L hemi-trees were significantly smaller compared with the permuted values (Z-scores of -2.94 ± 2.6 ; p values were <0.05 in 80% of cases). Moreover, when we plotted the Pearson correlation matrices of peri-behavioral event time segments for different behavioral events, we found marked differences in the dendritic compartmentalization between different behavioral events for both tasks (fig. S11), further indicating differential spatial dendritic representation of various motor events.

By contrast, GLM analysis for type 2 PTNs revealed a more uniform encoding of motor variables along the tuft and only minimal correlation to the tuft tree structure (Fig. 5, K to T). Although the GLM vectors for the different ROIs of the same single neuron were not completely identical, we did not observe systematic differences between or within the hemi-trees (Fig. 5, V and W; comparison of experimental and permuted random ROI locations yielded Z-scores of -0.47 ± 1.72 ; p values were <0.05 in 27% of cases; $p < 0.01$ comparing between Z-scores of type 1 and type 2 PTNs, Wilcoxon rank test).

To understand the impact of the differential tuft activity on the output of type 1 and type 2 PTNs, we performed tuft and soma imaging from the same neurons. We hypothesized that the combined computational products of the hemi-trees will affect the representation of motor variables at the soma. Indeed, GLM modeling of the somatic activity revealed a composite tuning that reflected the summed representation of both hemi-trees for type 1 and 2 PTNs (Fig. 5, B and L, and fig. S12). We found high Pearson correlation coefficients between the GLM vectors of the R/L tuft ROIs and the corresponding somas for type 1 and even more so for type 2 PTNs (Fig. 5X).

To further investigate the mechanisms underlying the observed activity in vivo, we performed modeling experiments on reconstructed type 1 and type 2 PTNs using the neuron platform (Fig. 6). We activated the tuft tree with pseudorandom patterned inputs (Fig. 6, A to C) and in vivo-like activation frequencies (43, 44). Compatible with our in vivo results, we could readily observe

R/L hemi-tree separation and compartmental calcium responses within hemi-tree tuft branches in a type 1 (Fig. 6C; compare Fig. 6D and Fig. 2, C to E, and movies S7 to S10; same neuron as in Fig. 2, A to E) but not in type 2 PTNs (fig. S13; same neuron as in Fig. 3, A to C). However, the in vivo results showed a higher intercorrelation within terminal subtrees for clusters 2 and 3 events, probably reflecting a nonrandom input distribution on the tuft tree in vivo (fig. S14, A and B). The simulated voltage correlation matrices also captured the main features of the tuft tree segmentation (Fig. 6F). Yet, the voltage signals showed higher correlations than the calcium signals, reflecting the localized calcium influx to the synaptic sites (via NMDAR) and the high-pass filtering effect of voltage-gated calcium channels (VGCCs) [see also Lavzin *et al.* (45)].

Next, we used our simulations to characterize the nature of the calcium event clusters. In type 1 PTNs, the four clusters differed primarily in the degree of recruitment of the NMDAR spiking mechanism (Fig. 6E). In type 2 PTNs, massive and widespread recruitment of NMDA spikes already occurred in cluster 2 events (fig. S13, D and H). Consistent with the critical role of NMDAR spiking mechanisms in replicating the in vivo findings, simulations with AMPAR-only synapses (Fig. 6B) failed to generate significant tuft activation (46). These results agree with our experimental demonstration of a marked reduction in the calcium activity of tuft dendrites after NMDAR blockade (fig. S8). We then investigated the contribution of VGCCs to tuft compartmentalization in type 1 PTNs. Elimination of VGCCs from the nexus had little impact on tuft segmentation, except for cluster 4 events, where removal of VGCCs increased R/L hemi-tree segmentation (Fig. 6G). Taken together, our simulations show that tuft segmentation is primarily dependent on differential recruitment of NMDAR spiking mechanisms in different tuft branches, and VGCCs play a minimal role in this process.

Because we could replicate the major characteristics of our experimental results with pseudo-random input patterns in both type 1 and 2 PTNs, we hypothesized that the distinct degrees of tuft segmentation must be linked to the difference in dendritic morphology, especially nexus size. To investigate this hypothesis, we scaled down the size of the apical arbor of the type 1 PTN but kept the soma-tuft distance unchanged. Under these conditions, we observed a sharp reduction in the segmentation within and between the hemi-trees (Fig. 6, H and I). This conclusion is further supported by our voltage simulations, which show that dendritic independence was primarily driven by the sizable electrotonic distance along the nexus (fig. S14C) and by the decreased NMDAR-dependent nonlinear interactions as a function

of the distance between dendritic locations, with only minimal interactions between the two hemitrees [fig. S14D; see also Kerlin *et al.* (11)].

Discussion

Overall, our results reveal a subclass of thick-tufted layer 5 PTNs in M1 (type 1) that performs parallel independent representations of motor information within its tuft dendrites. The degree of tuft compartmentalization was primarily dependent on the nexus and tuft tree morphology and required the NMDA spiking mechanism. In these neurons, motor information is integrated and amplified via NMDA spikes within adjustable segments of the tuft, ranging from small tertiary and quarterly sister branches, independent R/L hemi-trees, and up to a single global computational compartment in the minority of events. Our modeling suggests that calcium spikes play only a minimal role in tuft compartmentalization and local amplification. Instead, the initiation of calcium spikes in the distal apical trunk and proximal nexus branches probably serves to further amplify the tuft computational products (46, 47).

Type 2 PTNs also amplify behaviorally relevant motor information within their tuft but in a more global manner, mostly functioning as a single computational compartment (8–11).

The type 1 subclass constitutes a sizable fraction of thick-tufted layer 5 PTNs (~40%), in line with previous reports (24, 26). Although we based our classification solely on the apical dendritic morphology, our physiological findings supported this classification. Studies that examined both dendritic morphology and projection targets suggest that type 1 PTNs may preferentially project to the medulla (23, 27, 32), which is consistent with our medulla and spinal cord retrograde-labeled PTNs. Further studies are required to examine the projection pattern and molecular markers of type 1 and 2 PTNs (23, 32).

Our results reconcile the differences in the findings of prior *in vitro* and modeling studies, which predicted the capacity of dendrites to compartmentalize information (4, 17, 22, 48, 49) and recent recordings from behaving mice, which show that tuft dendrites function primarily as a single global amplification unit (8–11). Several past studies also observed infrequent local spikes that were limited to small, non-overlapping dendritic segments in tuft dendrites (9–11). Yet, this highly localized spiking activity, reminiscent of our cluster 1 events, cannot serve for efficiently communicating tuft computations to the soma. It may be used for local plasticity instead (6, 21). A study (6) that recorded tuft dendrites of M1 layer 5 PTNs reported spatially isolated dendritic spikes in almost all pairs of sibling distal tuft branches (95%). The results of this study dif-

fer from ours, as we observed selective activation of sibling terminal tuft branches during both motor tasks infrequently (<5%). These results are especially surprising in the case of type 2 layer 5 PTNs, which should have also been observed in that study. The discrepancies between our findings and those of (6) were probably related technical issues such as the low acquisition rate and the lack of adequate sparse labeling in (6).

The R/L hemi-tree compartmentalization is perhaps one of the most distinctive and intriguing properties of type 1 PTNs, which was not anticipated from previous work. This hemi-tree tuft compartmentalization enables PTNs to represent different sets of information in parallel, with each hemi-tree routing information to the soma independently acting as “a neuron within a neuron.” It is conceivable that in larger and more complex primate and human PTNs, this property would have an even larger impact, with a greater number of almost isolated integrative zones in the tuft (50, 51).

On the basis of our data, we propose a new integration and representation scheme of motor variables in tuft dendrites of M1 layer 5 PTNs. Motor variables are not represented in fully compartmentalized, small, nonoverlapping dendritic segments as previously reported (6). Instead, a given motor behavior or a sequence is represented by the activation of a specific combination of distal tuft segments, which are mutually coamplified via NMDA spikes to form spatial dendritic amplification maps for different motor behaviors. In this framework, the tuft tree of type 1 layer 5 PTNs is capable of dynamic combinatorial representation of a large number of motor variables and sequences within the same dendritic tuft branches (2, 52, 53).

REFERENCES AND NOTES

1. T. Branco, M. Häusser, *Curr. Opin. Neurobiol.* **20**, 494–502 (2010).
2. X. E. Wu, B. W. Mel, *Neuron* **62**, 31–41 (2009).
3. G. J. Stuart, N. Spruston, *Nat. Neurosci.* **18**, 1713–1721 (2015).
4. G. Major, M. E. Larkum, J. Schiller, *Annu. Rev. Neurosci.* **36**, 1–24 (2013).
5. S. D. Antic, W. L. Zhou, A. R. Moore, S. M. Short, K. D. Ikonomu, *J. Neurosci. Res.* **88**, 2991–3001 (2010).
6. J. Cichon, W. B. Gan, *Nature* **520**, 180–185 (2015).
7. L. M. Palmer *et al.*, *Nat. Neurosci.* **17**, 383–390 (2014).
8. L. Beaulieu-Laroche, E. H. S. Toloza, N. J. Brown, M. T. Harnett, *Neuron* **103**, 235–241.e4 (2019).
9. V. Francioni, Z. Padamsey, N. L. Rochefort, *eLife* **8**, e49145 (2019).
10. J. Voigts, M. T. Harnett, *Neuron* **105**, 237–245.e4 (2020).
11. A. Kerlin *et al.*, *eLife* **8**, e46966 (2019).
12. N. L. Xu *et al.*, *Nature* **492**, 247–251 (2012).
13. C. O. Lacefield, E. A. Pnevmatikakis, L. Paninski, R. M. Bruno, *Cell Rep.* **26**, 2000–2008.e2 (2019).
14. B. B. Ujfalussy, J. K. Makara, M. Lengyel, T. Branco, *Neuron* **100**, 579–592.e5 (2018).
15. R. Naud, B. Bathellier, W. Gerstner, *Front. Comput. Neurosci.* **8**, 90 (2014).
16. P. Poirazi, T. Brannon, B. W. Mel, *Neuron* **37**, 989–999 (2003).
17. D. Beniaguev, I. Segev, M. London, *Neuron* **109**, 2727–2739.e3 (2021).

18. A. Payeur, J. C. Béique, R. Naud, *Curr. Opin. Neurobiol.* **58**, 78–85 (2019).
19. G. Kastellakis, P. Poirazi, *Front. Mol. Neurosci.* **12**, 300 (2019).
20. R. Legenstein, W. Maass, *J. Neurosci.* **31**, 10787–10802 (2011).
21. J. Bono, C. Clopath, *Nat. Commun.* **8**, 706 (2017).
22. B. W. Mel, in *Advances in Neural Information Processing Systems*, J. Moody, S. Hanson, R. Lippmann, Eds. (Morgan Kaufmann, 1992), vol. 4, pp. 35–42.
23. M. N. Economo *et al.*, *Nature* **563**, 79–84 (2018).
24. H. Markram *et al.*, *Cell* **163**, 456–492 (2015).
25. W. J. Gao, Z. H. Zheng, *J. Comp. Neurol.* **476**, 174–185 (2004).
26. Y. Wang, M. Ye, X. Kuang, Y. Li, S. Hu, *IBRO Rep.* **5**, 74–90 (2018).
27. S. Jiang *et al.*, *Sci. Rep.* **10**, 7916 (2020).
28. G. M. Shepherd, *Nat. Rev. Neurosci.* **14**, 278–291 (2013).
29. A. Groh *et al.*, *Cereb. Cortex* **20**, 826–836 (2010).
30. E. J. Kim, A. L. Juavinett, E. M. Kyubwa, M. W. Jacobs, E. M. Callaway, *Neuron* **88**, 1253–1267 (2015).
31. A. M. Hattox, S. B. Nelson, *J. Neurophysiol.* **98**, 3330–3340 (2007).
32. B. Tasic *et al.*, *Nature* **563**, 72–78 (2018).
33. L. N. Fletcher, S. R. Williams, *Neuron* **101**, 76–90.e4 (2019).
34. S. Levy *et al.*, *Neuron* **107**, 954–971.e9 (2020).
35. F. Fuhrmann *et al.*, *Neuron* **86**, 1253–1264 (2015).
36. T. W. Chen *et al.*, *Nature* **499**, 295–300 (2013).
37. T. Deneux *et al.*, *Nat. Commun.* **7**, 12190 (2016).
38. N. Mantel, *Cancer Res.* **27**, 209–220 (1967).
39. B. Manly, *The Statistics of Natural Selection* (Chapman & Hall, 1985).
40. P. W. Mielke, *Biometrics* **34**, 277 (1978).
41. B. Engelhard *et al.*, *Nature* **570**, 509–513 (2019).
42. P. Ramkumar, B. Dekleva, S. Cooler, L. Miller, K. Kording, *PLOS ONE* **11**, e0160851 (2016).
43. B. A. Sauerbrel *et al.*, *Nature* **577**, 386–391 (2020).
44. A. Nashef, O. Cohen, R. Harel, Z. Israel, Y. Prut, *Cell Rep.* **27**, 2608–2619.e4 (2019).
45. M. Lavzin, S. Rapoport, A. Polsky, L. Garion, J. Schiller, *Nature* **490**, 397–401 (2012).
46. M. E. Larkum, T. Nevian, M. Sandler, A. Polsky, J. Schiller, *Science* **325**, 756–760 (2009).
47. M. Larkum, *Trends Neurosci.* **36**, 141–151 (2013).
48. H. Jia, N. L. Rochefort, X. Chen, A. Konnerth, *Nature* **464**, 1307–1312 (2010).
49. M. E. Sheffield, D. A. Dombeck, *Nature* **517**, 200–204 (2015).
50. L. Beaulieu-Laroche *et al.*, *Cell* **175**, 643–651.e14 (2018).
51. H. Mohan *et al.*, *Cereb. Cortex* **25**, 4839–4853 (2015).
52. R. Urbanczik, W. Senn, *Neuron* **81**, 521–528 (2014).
53. J. Hawkins, S. Ahmad, *Front. Neural Circuits* **10**, 23 (2016).

ACKNOWLEDGMENTS

We thank S. Marom and B. Engelhard for helpful comments on the manuscript. We also thank S. Schwartz for advice in statistical tests and S. Gafniel for movie editing. **Funding:** This study was partially supported by the Israeli Science Foundation (J.S. and Y.S.), Prince funds (J.S. and Y.S.), Rappaport Foundation (J.S. and Y.S.), and Zuckerman Postdoctoral Fellowship (N.C.). **Author contributions:** Designed research: J.S., N.C., Y.S. Performed experiments: Y.O., N.C., S.A., M.A. Analyzed data: S.A., Y.O., J.S., H.B., O.B., Y.S. Writing – original draft: J.S. Writing – review and editing: J.S., Y.O., S.A., A.P.-P., Y.S. Performed simulations: A.P.-P., S.A., J.S. **Competing interests:** The authors declare that they have no competing interests. **Data and materials availability:** All data are available in the manuscript or the supplementary materials. Computer code can be found in: <https://github.com/SchillersLab/Dynamic-compartmental-computations-in-tuft-dendrites>.

SUPPLEMENTARY MATERIALS

science.org/doi/10.1126/science.abn1421
Materials and Methods
Figs. S1 to S14
References (54–60)
MDAR Reproducibility Checklist
Movies S1 to S10

[View/request a protocol for this paper from Bio-protocol.](#)

7 November 2021; accepted 11 March 2022
10.1126/science.abn1421



Dynamic compartmental computations in tuft dendrites of layer 5 neurons during motor behavior

Yara Otor, Shay Achvat, Nathan Cermak, Hadas Benisty, Maisan Abboud, Omri Barak, Yitzhak Schiller, Alon Poleg-Polsky, and Jackie Schiller

Science **376** (6590), . DOI: 10.1126/science.abn1421

Independent computations within dendrites

Cortical pyramidal neurons typically have an elaborate dendritic tree that receives and integrates the many synaptic inputs targeting the neuron. An open question is how information is represented in dendrites in vivo. Otor *et al.* investigated synaptic computations in the apical tuft of layer 5 pyramidal neurons in the mouse motor cortex using two-photon calcium imaging, behavioral analysis, and cable modeling. Early-branching layer 5 pyramidal neurons showed marked compartmentalization of dendritic calcium signaling, whereas late-branching pyramidal neurons had synchronous tuft activation. *N*-methyl-d-aspartate spikes and cable properties could explain the varying compartmentalization patterns. Compartmentalized activity between hemi-trees was correlated with behavioral outcome. These results indicate a cell-type-dependent dynamic combinatorial code for motor representation. —PRS

View the article online

<https://www.science.org/doi/10.1126/science.abn1421>

Permissions

<https://www.science.org/help/reprints-and-permissions>

Use of this article is subject to the [Terms of service](#)

Science (ISSN 1095-9203) is published by the American Association for the Advancement of Science. 1200 New York Avenue NW, Washington, DC 20005. The title *Science* is a registered trademark of AAAS.

Copyright © 2022 The Authors, some rights reserved; exclusive licensee American Association for the Advancement of Science. No claim to original U.S. Government Works



Supplementary Materials for

Dynamic compartmental computations in tuft dendrites of layer 5 neurons during motor behavior

Yara Otor *et al.*

Corresponding authors: Alon Poleg-Polsky, alon.poleg-polsky@cuanschutz.edu; Jackie Schiller, jackie@technion.ac.il

Science **376**, 267 (2022)
DOI: 10.1126/science.abn1421

The PDF file includes:

Materials and Methods
Figs. S1 to S14
References

Other Supplementary Material for this manuscript includes the following:

MDAR Reproducibility Checklist
Movies S1 to S10

Methods

Experimental model

All animal procedures were performed in accordance with guidelines established by the NIH on the care and use of animals in research, as confirmed by the Technion Institutional Animal Care and Use Committee. Adult C57BL mice were used in this study. Animals were housed in a 12:12 hours reverse light:dark cycle. For behavioral training and experiments, food intake was limited to 2.8–3 g/day with *ad libitum* water.

Surgical preparation

Surgical procedures were performed under isoflurane anesthesia (4% for induction and 1.5-2% during surgery). Mice aged 8-12 weeks were anesthetized and secured in a stereotaxic apparatus. A heat pad was used to maintain body temperature at 36-37 °C. The scalp was shaved and cleaned with iodine solution and ethanol. The skull surface was exposed after a subcutaneous injection of 2% Lidocaine. A small circular craniotomy (2.5 – 3 mm diameter) was performed for viral injections over the primary motor cortex forelimb area 0.6 mm anterior and 1.6 mm lateral to Bregma, defined by optogenetic inhibition as described previously (34). For sparse labeling of layer-5 PTNs, we injected a mixture of a diluted AAV carrying Cre recombinase either under the CamKII promoter (AAV1-CamKII0.4-Cre-SV40; Addgene viral prep # 105558-AAV1, final titer roughly 1.8×10^8 genome copies per milliliter) or under the PT promoter (AiP1010-pAAV-mscRE4-minBGpromoter-iCre-WPRE-hGHpA; Addgene plasmid # 163476 (54)) and a concentrated AAV carrying flexed GCaMP6s and mRuby2 (AAV1-CAG-Flex-mRuby2-GSG-P2A-GCaMP6s-WPRE-pA; Addgene viral prep # 68717-AAV1, titer roughly 1×10^{13} genome copies per milliliter) or flexed GCaMP6f and mRuby2 (AAV1-CAG-Flex-mRuby2-GSG-P2A-GCaMP6f-WPRE-pA; Addgene viral prep # 68719-AAV1, titer roughly 1×10^{13} genome copies per milliliter). 50nL of the

virus mixture was injected using a hydraulic micromanipulator (M0-10 Narishige) at several sites within the craniotomy at 750 μm below dura. After the injections, an optical window constructed from a 2.5 mm and 3.5mm 170 μm thick circular glass disks glued together was placed over the exposed brain and superglued in place. A custom-made 3D printed headpost (34) was affixed to the skull using dental cement.

Injections of ketoprophen (5 mg/kg) and buprenorphine (0.1 mg/kg) were administered subcutaneously for analgesia during surgery and for 2-days post operation. Mice recovered for at least one week following surgery with *ad libitum* food and water.

Retrograde spinal cord and medulla labeling of PTNs

For spinal cord retrograde labeling of PTNs, we performed a laminectomy at C2-C3 level and injected contralaterally a mixture of AAV-retro viruses: pENN.AAV.hSyn.Cre.WPRE.hGH (diluted to titer 0.9×10^{10}), pAAV-FLEX-tdTomato (titer 2.6×10^{13}) and pGP-AAV-CAG-FLEX-jGCaMP7s-WPRE (titer 1.1×10^{13}) through the dura, lateral to the midline at depths 800 μm , 600 μm and 400 μm from dura. For medulla retrograde labeling of PTNs, same viruses were injected to the contralateral medulla (0.9 ML, 6.6 AP) at depths 4.6 mm and 5 mm from the dura. Neurons were reconstructed from M1 region.

Pharmacological blocker application

For experiments with local injection of pharmacological blockers, we used a cranial window with a drilled access hole sealed with biocompatible silicone (55). The blockers were injected using a hydraulic micromanipulator with a glass pipette that was inserted into the cortex with an angle to reach the specific imaged region of interest, typically at a vertical depth of $\sim 150 \mu\text{m}$ from dura. Approximately 500 nl of MK801 (80 μM) was injected. The experiments started 5 min after the injection of the blocker and lasted for 30 min. This duration was chosen based on the estimated

half-time clearance rate of the drugs, determined from analysis of the fluorescence decay of Alexa fluor-594, which is a similar-sized water-soluble.

Behavioral training

For the hand reach experiments, mice were restricted to 2.8–3 g/day of food with *ad libitum* water. Training started when the animals reached 85-90% of their original body weight. Mice were habituated to head fixation in a custom-built apparatus (34) in dark and quiet conditions, monitored by a webcam. Mice were initially trained to retrieve food pellets (14 mg; Test Diet; St Louis, MO) from a rotating plate placed directly below the mouth. The plate was rotated every 45 sec using either a NI USB DAQ device or a Teensy microcontroller driven by custom-made LabVIEW software to present a food pellet. An auditory tone (200 ms, 1 kHz) was used as a cue during plate rotation. Mice were trained until they routinely responded to the auditory cue and grabbed the food pellet with at least 50% success rate (34); thereafter behavior was combined with two-photon imaging. We took care to reproduce the location of the pellet across sessions.

For the treadmill experiments, head-fixed mice were trained to run freely on a linear treadmill (Luigs & Neumann) positioned under the microscope. Treadmill belt motion was recorded during imaging via a rotary encoder. Mice typically learned to initiate running on treadmill within a single 30 min training session.

Treadmill position and two-photon recordings were synchronized by recording the two-photon imaging frame trigger signal, simultaneously with the treadmill encoder on a single machine using either an NI USB DAQ device or a Teensy microcontroller.

Two-photon calcium imaging

Images were acquired using a two-photon microscope (Bruker 2P-Plus) equipped with a dual-beam Insight X3 laser (Spectra Physics), an 8 kHz bidirectional resonant galvo scanner and a

Nikon 16X CFI Plan Fluorite objective (NA 0.8), controlled by the software package PrairieView 5.3. Fluorescence was split by a 565LP dichroic and filtered with 525/70 and 595/50 bandpass filters before collection on two GaAsP photomultiplier tubes (Hamamatsu H10770PB-40 and H11706-40, respectively) to image the red (mRuby2) and green (GCaMP6) fluorescent markers. For single plane imaging, the imaging region was $\sim 400 \times 400 \mu\text{m}$, either 512×512 pixels at a frame rate of 30 Hz or 768×768 pixels at a rate of 20 Hz. For quasi-simultaneous two plane soma-tuft imaging, we used an electrically tunable lens (ETL), and the imaging region was $\sim 400 \times 400 \mu\text{m}$, 512×512 pixels at $\sim 10\text{Hz}$ acquisition rate. Illumination was centered at a wavelength of 940 nm with 30-40 mW mean power at the objective. PMT gains were set to minimize saturated pixels during calcium transients. For the hand reach experiments, each trial lasted for 12 sec with the tone and plate rotation introduced 4 sec after the start of the trial. Inter-trial intervals were typically 30 sec, and a total of 50-120 trials were collected per session. Behavioral performance was monitored at 200 Hz using two cameras (side and front view; Flea3 FL3-U3-13Y3M, PointGrey). For the treadmill experiments, to minimize photobleaching, we acquired images in segments of 30 sec followed by an inter-acquisition interval of 15 sec. The total imaging period was 30 min per session.

Two-photon dendritic structural imaging

For structural imaging, head-fixed mice were anaesthetized with 1-2% isoflurane and placed over a heat pad to maintain body temperature. We recorded large field of view volumetric z-stacks ($750 \times 750 \mu\text{m}$, 1536×1536 pixels, $3 \mu\text{m}$ axial spacing for tuft and $10 \mu\text{m}$ for apical regions) of mRuby2 fluorescence using 1045 nm two-photon illumination with Galvo scanners at a $10 \mu\text{sec}$ dwell time per pixel.

Quantification and statistical analysis

Unless otherwise specified, the data were analyzed using custom Matlab, R, or Python scripts.

Behavioral data analysis

We used both a modified version of the Janelia Automatic Animal Behavior Annotator (JAABA) software package (56) to classify behavioral events and machine-learning-based algorithm DeepLabCut (57), to automatically track the hand position from our behavioral videos. For behavioral annotations using JAABA software, the hand reach task was segmented into discrete behavioral events (lift, grab, supination, at mouth and back to perch). A subset of trials was manually labeled to train the classifier to recognize the behavioral events of interest. Then, machine-learning-based classified behavioral events were extracted from all trials. The events were defined as follows: lift is defined from the initial separation between hand and perch until the hand reaches maximum height, grab is defined from the beginning of fingers closure until the hand was lifted off the table (with or without the pellet), supination is defined when the paw starts rotating until it faces upward, at mouth is defined as the hand with a pellet in close proximity to mouth, back to perch was the downward movement of the paw.

Success trials were defined as trials where mice succeeded in grabbing and bringing the food pellet to the mouth for consumption (regardless of how many grab attempts were made). Failure trials were defined as trials where mice attempted to grab but missed the food pellet and thus did not consume it.

On each trial, X and Y locations of the hand were automatically extracted from the videos of the side and front cameras using DeepLabCut (57), where a small subset of video frames was automatically extracted for training the software.

For treadmill experiments, movement information was extracted from the belt motion via a rotary encoder.

Two-photon data analysis

The fluorescence data acquired by the two-photon microscope were first registered to correct for brain motion artifacts. Our registration method was based on Fienup, J. & Kowalczyk (58), using Fourier transform-based correlation between two successive images. The maximal value position in the correlation image specifies the relative shift between the two images; we designate them u_t and v_t . This method required a template specification and matching against an image stack. The template image $I_{temp}(x, y)$ was defined as the average of all images in the selected trial over time.

$$I_{temp}(x, y) = \frac{1}{N} \sum_{t=1..N} I(x - u_t, y - v_t, t) \quad (1)$$

The set $\{u_t, v_t\}, t = 1..N$ is an image shifted in the XY plane after alignment. We initially started with $u_t=0, v_t=0$ and then updated their values according to the registration maxima. This procedure was repeated several times. In each iteration, when each time we computed a new template $I_{temp}(x, y)$ using previously computed $\{u_t, v_t\}$ for each image. Typically, this procedure converges after several iterations, in our case three iterations.

To align the imaging data over many trials, we used a similar technique, utilizing the previously computed averaged templates for each trial. For each trial k , we performed a single trial registration using the template algorithm for three iterations. To align the image data over many trials, we treated the final templates $I_{temp}^k(x, y)$ from each trial k as unaligned image data and repeated the same registration procedure to find offsets $\{u_k, v_k\}$ for each trial. These offsets, along with previously found offsets $\{u_t, v_t\}$, account for the final image shift in the XY plane.

Regions of interest (ROIs) were detected manually using average fluorescence images and $\Delta F/F$ projection images, which highlighted active neurons. The pixels within each ROI were averaged

for every frame. The ROI "mask" was used to detect the same neurons on multiple imaging sessions on different days.

$\Delta F/F$ was computed using the following formula:

$$\Delta F/F_n [t] = \frac{F_n[t] - \text{Min}10(F_n[t])}{\text{Min}10(F_n[t]) + \text{Bias}} \quad (2)$$

$\text{Min}10(F_n [t])$ is a mean value of the lowest consecutive 10% values of the fluorescence signal $F_n [t]$. This minimal fluorescence value was calculated both per trial and across the entire experimental session, with no significant differences in the results with these two calculation variants. A small bias factor in the denominator prevented division by zero when the cell was completely silent.

Care was taken to include in the analysis only dendritic ROIs which were in focus with the imaging plane as determined by the red channel. On average, we sampled a similar percent of terminal branches from type-1 and type-2 PTNs ($81.1 \pm 11\%$ and $80.1 \pm 0.01\%$; $p=0.84$ for type-1 and type-2 PTNs respectively). The average SNR of the calcium fluorescence signal was 7.5 ± 2.9 dB and 8.2 ± 2.6 dB for type-1 and type-2 PTNs respectively ($p=0.17$).

Structural Organization Analysis

Morphological Reconstruction of Cells. Our sparse transfection method resulted in only few layer-5 PTNs in each field of view ($\sim 400 \times 400 \mu\text{m}$; on average 1.6 ± 0.85 neurons, $n=28$ animals). We used the Simple Neurite Tracer plugin in Fiji software to reconstruct the entire tuft and apical dendrite morphology up to the soma. Basal and oblique dendrites were not reconstructed fully due to insufficient resolution; hence they were not depicted on the figures. NeuroAnatomy Toolbox v1.5.2 was used to align the imaged ROIs onto the reconstructed tuft tree structure.

Hierarchical clustering. We used 5 anatomical measures to cluster the thick-tufted layer-5 PTNs (hierarchical clustering linkage function with Ward): Nexus size (the summed distance between first and second bifurcations of the two primary tuft branches); First bifurcation depth from pia; Second bifurcation depth from pia, right branch; Second bifurcation depth from pia, left branch; Soma depth from pia. The number of clusters was validated using the internal clustering validation Calinski-Harabasz index and was consistent with the number of 2.

Structural distance-matrix. Based on the reconstructed data, we represented each cell as a tree structure reflecting the anatomical hierarchy, where nodes are branches and end-points and edges reflect dendritic branch points, weighted by the length of each branch (Euclidian distance in X-Y-Z plane). To obtain a matrix of distances between ROI's, we evaluated the pairwise distances between ROIs of each cell as the shortest Euclidian path (in μm) on the tree for traveling from one node to another, organized according to the tree structure.

Event detection and clustering. For each ROI, all trial repetitions in a session were concatenated into a single time trace denoted by $x_i(t)$, where $i = 1, 2, \dots, N$ enumerates the ROIs and t stands for time samples. Calcium transients ($\Delta F/F$) were detected using a modified MLSpike software (37). Using the MLSpike software, we identified dendritic events by the shape of the events (abrupt increase and gradual reduction of the $\Delta F/F$). In contrast to somatic action potentials, dendritic spikes are graded and not composed of single or multiple unitary events. Thus, we did not transform the calcium data to spike trains. Our detector defined calcium transients as single events as long as the $\Delta F/F$ did not decrease by at least 25% of the peak amplitude. The reliability of event detection was validated with human-based detection in several experiments.

To classify the calcium transients in the different ROIs to different clusters by their peak, we assigned each transient to a specific "calcium event" by the average peak across all ROIs. We

defined all calcium transients occurring simultaneously as belonging to the same “event”. The average calcium signal trace was calculated by the mean values (over time) across the calcium signals in all ROIs. The peak amplitude of each calcium event was classified according to the peak of the average calcium trace in the corresponding time window. For each experiment, we used the k-means algorithm to divide our events to 4 clusters based on these peak amplitudes. A second method we used to sort the calcium events to the 4 clusters was according to the number of ROIs which were active during each event, thus directly determining the spatial extent of the dendritic activation.

Events correlation matrix. We constructed a correlation matrix related to each calcium event cluster as follows: we extracted the activity in the time window from the onset to the peak of the events from all ROIs belonging to that cluster. These events were concatenated to a vector across time to obtain X_k , a matrix of $N \times T_k$ where T_k is the number of the total time samples extracted for cluster k . We evaluated the Pearson correlation between all pairwise combinations of ROIs (per neuron) resulting in an $N \times N$ matrix. We sorted the rows and columns of these matrices according to the ROIs order in the tree to obtain an activity correlation matrix and to produce a scatter plot of pairwise Pearson correlation values vs. the shortest physical path. Correlations were calculated only for events that occurred at least in one of the ROIs.

Statistical Analysis

Structural-functional correlations.

2D PCA embedding of calcium signals. All calcium events were concatenated for each ROI, resulting in an $N \times T$ matrix denoted as Y , comprising the activity of N ROIs in T time samples.

We used principal component analysis (PCA) to represent each ROI in a lower dimensional space with respect to the temporal axis. We evaluated the sample covariance of Y by

$$C = Y^T Y \quad (3)$$

and applied eigenvalue decomposition

$$C v_l = \mu_l v_l$$

$$l = 1, \dots, T \quad (4)$$

where v_l are the eigenvectors with the associated μ_l eigenvalues. The eigenvectors of the sample covariance give rise to the principal components of the imaging data matrix Y with respect to the temporal axis.

We used the first two principal components (related to the largest eigenvalues) of each ROI, $(v_l(1), v_l(2)), n = 1, \dots, N$, to visualize the ROIs in a two-dimensional principal component (PC) space.

Hemi-tree compartmentalization. We estimated the significance of R/L hemi-tree segregation of the Pearson correlation values using shuffling of the within and between hemi-tree labels. For each experiment, we calculated the difference between the mean pairwise Pearson correlations of within compared to between hemi-trees ROIs ($\text{Mean}_{\text{within}} - \text{Mean}_{\text{between}}$). Next, we shuffled the “within” and “between” labels of each pair-wise Pearson correlation coefficient value over 1000 perturbations and calculated the Z-score of the experimental values from the shuffled distribution.

Mantel Test. To test the degree of similarity between the structure of the tree and its activity, we performed a Mantel test (38) between the structural and the event correlation matrices for each cluster. We used 5,000 permutations to estimate the null distribution and p-values.

Goodness of fit - R^2 and slope for the linear regression model. To quantify the correlation between activity and distance between the ROIs in the tree, we calculated the R^2 of the Pearson values as a function of tree distance with a linear regression where we predict Pearson values using a single (distance) predictor model (glmfit in Matlab). The significance of R^2 was calculated using 1,000-fold shuffles (permutations) of the dendritic distance values. The p-value was the proportion of permuted R^2 which was greater than the experimental value.

The slope was calculated using the linear prediction model after normalizing the maximum distance value to 1 for each tuft tree.

ANOVA Test. We used one-way ANOVA to compare between four event clusters for R^2 entire tree, R^2 hemi-tree, the slope of the linear regression and Mantel values. We performed post hoc analysis using Tukey-Kramer correction to measure between-group significance.

Wilcoxon test. A-parametric independent sample Wilcoxon test (ranksum in Matlab) was used for evaluating the statistical significance between type-1 and type-2 PTNs for each cluster for the following: R^2 of Pearson linear regression in the entire tuft tree, R^2 in each hemi-tree, slope of the linear regression and Mantel values.

Generalized linear model.

Hand reach analysis - we modeled single ROI calcium transients using a generalized linear model (GLM)(34, 41, 42) based on behavioral variables serving as predictors.

The predictors were of four types:

1. Hand trajectories. Time series of hand trajectories were extracted using DeepLabCut (57) from videos taken with side and front view cameras. We extracted X and Y hand positions, altogether 4 predictors.

2. Orofacial features. Time series of orofacial motion variability features were extracted using FaceMap (59) from recorded videos. Facial movements were extracted from a single region covering the face for each view (side and front) and from each area the first 20 principal components were taken as predictors (34). Higher-order components had significantly lower relevance to behavioral and neuronal signals.
3. Time varying and binary events: tone, lift, grab, supination, at mouth and back to perch. The hand reach task was photographed using two high-speed video cameras (front and side view) and movement events were extracted using the modified JAABA software (56).
4. A whole trial binary event: success/failure trial outcome.

To model the time course of single-ROI calcium signals, we convolved the time-varying binary events with sets of 7 degrees-of-freedom regression splines generated using the ‘bSpline’ package in R. We used three sets of spline functions to account for different temporal durations (0.25, 0.5, 2 sec). We used 24 spline functions in total, which resulted in $24 \times 6 = 144$ convolved signals used as predictors. Altogether we had 189 predictors (144 convolved predictors + 4 hand trajectories + 40 orofacial features + 1 whole binary success/failure outcome status). We performed the analysis on a time window starting from 0.1sec before the tone to 3 (for well-trained mice) or 6 sec after the tone.

We trained a linear predictor for the neuronal activity of an ROI i based on the time traces of the predictors such that

$$\begin{pmatrix} x_{i,1}^T \\ x_{i,2}^T \\ \vdots \\ x_{i,T}^T \end{pmatrix} = AW_i + w_i^0 + \varepsilon_i \quad (5)$$

where $x_{i,k}^T$ is the time trace of neuronal activity of the i -th ROI on trial k , A is composed of the corresponding temporal predictor signals and $\{w_i, w_i^0\}$ are the evaluated model parameters. Our recordings of GCaMP neuronal signals, according to our empirical evaluations, reasonably match a normal distribution. Therefore, the link function required for the GLM is a unity function, rather than a logarithm function usually used for modeling spikes as Poisson processes. All models were trained per ROI using LASSO with 5-fold cross validation. Our data was somewhat better fitted by inverse Gaussian distribution and thus, we also performed the GLM analysis with the inverse-square link function. The fit of the GLM model with the experimental results was comparable using either Gaussian or inverse Gaussian distribution.

We first trained a full model based on all 189 predictors and measured $R_f^2(i)$, which is the variance of the estimated neuronal signal, divided by the variance of the recorded neuronal activity. For our further analysis, we included the subset of ROIs having at least 15% of their variance explained by the full model and excluded the rest from further analysis.

In order to quantify the relative contribution of each variable, we grouped the predictors into 9 categories: hand trajectories, orofacial features, tone, lift, grab, supination, at mouth, back to perch and outcome. We trained a set of nine partial models, each by excluding predictors related to one of the categories. The contribution of the excluded component was evaluated as:

$$\alpha(i, c) = 1 - \frac{R_p^2(i, c)}{R_f^2(i)} \quad c = 1, \dots, 9 \quad (6)$$

where $R_p^2(i, c)$ is the variance of the explained signal of the i -th ROI using the partial model $c=1, 2, \dots, 9$.

For some ROIs, the contribution was negative, indicating poor modeling due to noise or irrelevance of the predictors to the activity and therefore, the value was cropped to zero (41). The

relative contribution, $\alpha(i, c)/(\sum_{c=1}^9 \alpha(i, c))$ of each component c , averaged across ROIs in the hemi-trees.

Treadmill analysis – to quantify the contribution of behavioral variables to neuronal activity for treadmill experiments, we used a different set of predictors extracted from the belt motion via a rotary encoder.

- Continuous variables - position $x(t)$, speed, $v(t)$, acceleration $a(t)$. We also included v^2, v^3, a^2, a^3 to allow non-linear modeling between speed/acceleration and neuronal activity.
- Time-varying binary events - locomotion, quiescence, positive/negative acceleration and locomotion onsets and offsets.

To account for delays between binary events and calcium signal onset, we inserted built-in delays of ± 0.5 sec between the behavioral and imaging traces. To account for the time course of calcium transients, we convolved the binary traces using three sets of spline functions with a duration of 0.25, 0.5 and 2 sec, similar the hand reach task. Overall, we used 7 continuous predictors + 6 binary traces \times (2 delays + 24 spline functions) resulting in 163 predictors. GLM modeling was performed in the same manner as described for the hand-reach task, on locomotion and quiescence segments separately. Cross validation was performed by arbitrarily dividing the running/quiescence traces into 30 sec long trials.

Single neuron computer simulations

We used detailed morphological reconstructions of three neuronal morphologies to investigate the rules underlying the in vivo activity in tuft dendrites of the type-1 and -2 layer-5 PTNs. We converted the fluorescent z-stacks that were acquired in vivo to a morphometric format for multi-

compartment modeling using the NEURON 7 simulation platform. The locations of the experimental ROIs were saved and recreated in the simulation.

We constrained the range of the passive and active parameters in the simulation by the key features of thick-tufted layer-5 PTNs as reported in previous slice studies including: the degree of attenuation of voltages from tuft to nexus and from nexus to tuft (46, 60), the propagation of voltage and spread of calcium transients from nexus to the soma (9, 46, 60); the attenuation of calcium transients to the tuft evoked by nexus calcium spikes; the attenuation of voltage between the hemi-trees in type-1 PTNs (46).

Passive properties - The passive and active parameters were adapted from (45). The somatic resting membrane potential was set to -60 mV; membrane resistance to $20,000 \Omega \cdot \text{cm}^2$; the axial resistance was $80 \Omega \cdot \text{cm}$, and the membrane capacitance was set to $1.4 \mu\text{F}/\mu\text{m}^2$.

Active conductances along the dendritic tree - Active conductances were distributed as follows: Axon: HH-like sodium channel $50000 \text{ pS}/\mu\text{m}^2$; HH-like potassium channel $8000 \text{ pS}/\mu\text{m}^2$; KDR $10000 \text{ pS}/\mu\text{m}^2$. Soma: HH-like sodium channel $50 \text{ pS}/\mu\text{m}^2$; HH-like potassium channel $600 \text{ pS}/\mu\text{m}^2$; KDR $300 \text{ pS}/\mu\text{m}^2$; KA $1000 \text{ pS}/\mu\text{m}^2$; KM $20 \text{ pS}/\mu\text{m}^2$. The apical trunk: HH-like sodium channel $50 \text{ pS}/\mu\text{m}^2$; CaL $1 \text{ pS}/\mu\text{m}^2$; HH-like potassium channel $100 \text{ pS}/\mu\text{m}^2$; KDR $60 \text{ pS}/\mu\text{m}^2$; KA $1000 \text{ pS}/\mu\text{m}^2$; KCa $1 \text{ pS}/\mu\text{m}^2$. Apical tuft dendrites and basal dendrites: HH-like sodium channel $40 \text{ pS}/\mu\text{m}^2$; CaL $0.4 \text{ pS}/\mu\text{m}^2$; KDR $1 \text{ pS}/\mu\text{m}^2$; KA $30 \text{ pS}/\mu\text{m}^2$; KCa $10 \text{ pS}/\mu\text{m}^2$. IH was inserted in the tuft dendrites with $10 \text{ pS}/\mu\text{m}^2$ conductance. Apical sodium channels had a 10mV increase in the activation and deactivation kinetics. Nexus: was set as the dendritic region from first to second bifurcation with CaL $10 \text{ pS}/\mu\text{m}^2$.

The simulation included radial calcium diffusion in shells with buffers and longitudinal diffusion along the branches with a coefficient of $0.8 \mu\text{M}^2/\text{ms}$. Calcium pumps operated on the external shell, with a steady-state calcium concentration maintained at $100 \mu\text{M}$.

We calibrated the active conductance in the type-1 morphology to recreate the firing pattern and responses to dendritic stimulation recorded in vitro (45, 46). Nexus excitability was set to be sufficiently high to generate calcium spikes by dendritic current injection but not by a single back-propagating action potential. Tuft excitability was calibrated to restrict the propagation of nexus calcium spike back to the tuft. In simulations where we scaled down the nexus and tuft morphologies, we also increased the peak VGCC conductance value in the nexus proportionally by the change in dendrite length to maintain an invariant total calcium channel conductance.

Synapses - We simulated excitatory (AMPA, NMDAR) and inhibitory (GABAAR) synapses that reversed at 0 mV and -65 mV, respectively. AMPAR and GABAAR currents had an instantaneous rise time and a decay time of 2 and 7 ms. NMDAR currents had a rise time of 2 ms and a decay time of 50 ms. The voltage dependence of the NMDAR conductance was modeled as follows: $g_{\text{NMDA}} = 1/(1 + 0.25 \cdot \exp(-0.08 \cdot V_m))$ where V_m is the local membrane potential. The fractional NMDAR conductance was measured as the average g_{NMDA} value during each event. The fractional calcium conductance of the NMDARs was set to 0.01.

We used stimulation and background synapses. Background activity was implemented with 80 synapses (80% excitatory with synapse conductance = 0.7 nS, mean firing rate = 1 Hz; 20% inhibitory with synapse conductance = 1 nS, instantaneous rise time and a decay time of 7 ms, reversal potential of -65 mV and mean firing rate = 1 Hz) which were activated at random times and locations on the entire tuft and nexus region and were driven by a temporal pseudorandom pattern.

Pseu-dorandom activation: For simulations with a pseu-dorandom distribution of the signal-conveying synapses, we selected the number of active synaptic sites from a lognormal distribution with mean=60, SD=30. Synaptic size was chosen from a lognormal distribution with mean=SD=0.7 nS for both NMDA and AMPA receptors. The activation rate of these inputs increased and decreased over time by a Gaussian temporal envelope which specified their average firing rate at each time point. Presynaptic spiking rates rose from baseline (1 Hz) and peaked at 750 ms from the start of the trial to allow for stabilization of the simulation. The value for the peak was selected at random for each synapse to be either 20, 30 or 40 Hz. The temporal width of the synaptic activation (measured as the SD of the Gaussian) was 150 ms. The active synapses were reseeded with a unique spatiotemporal distribution pattern and conductance values for each simulation trial. Synaptic distribution over the arbor was achieved by drawing a random location from a uniform distribution mapped to the total dendritic length.

Patterened activation: In some simulations, we preferentially activated groups of preselected branches. Signal-conveying synapses were distributed either equally on all branches of a hemi-tree or preferentially distributed on same or neighboring terminal tuft branches. In patterned activations, synaptic strength was set to 0.7nS. The temporal presynaptic firing sequence for patterened activations was similar for all inputs, unique in each simulation run, and structured as described above, with a Gaussian envelope peaking at 40Hz firing rate.

Morphological alterations: Scaling down type-1 nexus and tuft: we shrunk the length of the nexus in our simulation by a factor of 6.82 and the length of all tuft branches by a factor of 2 to match the nexus/tree size of the simulated type-2 PTNs. In this manipulation, the length of the apical trunk was increased by 345 μm to maintain the total vertical size of the apical arbor.

Fig. S1

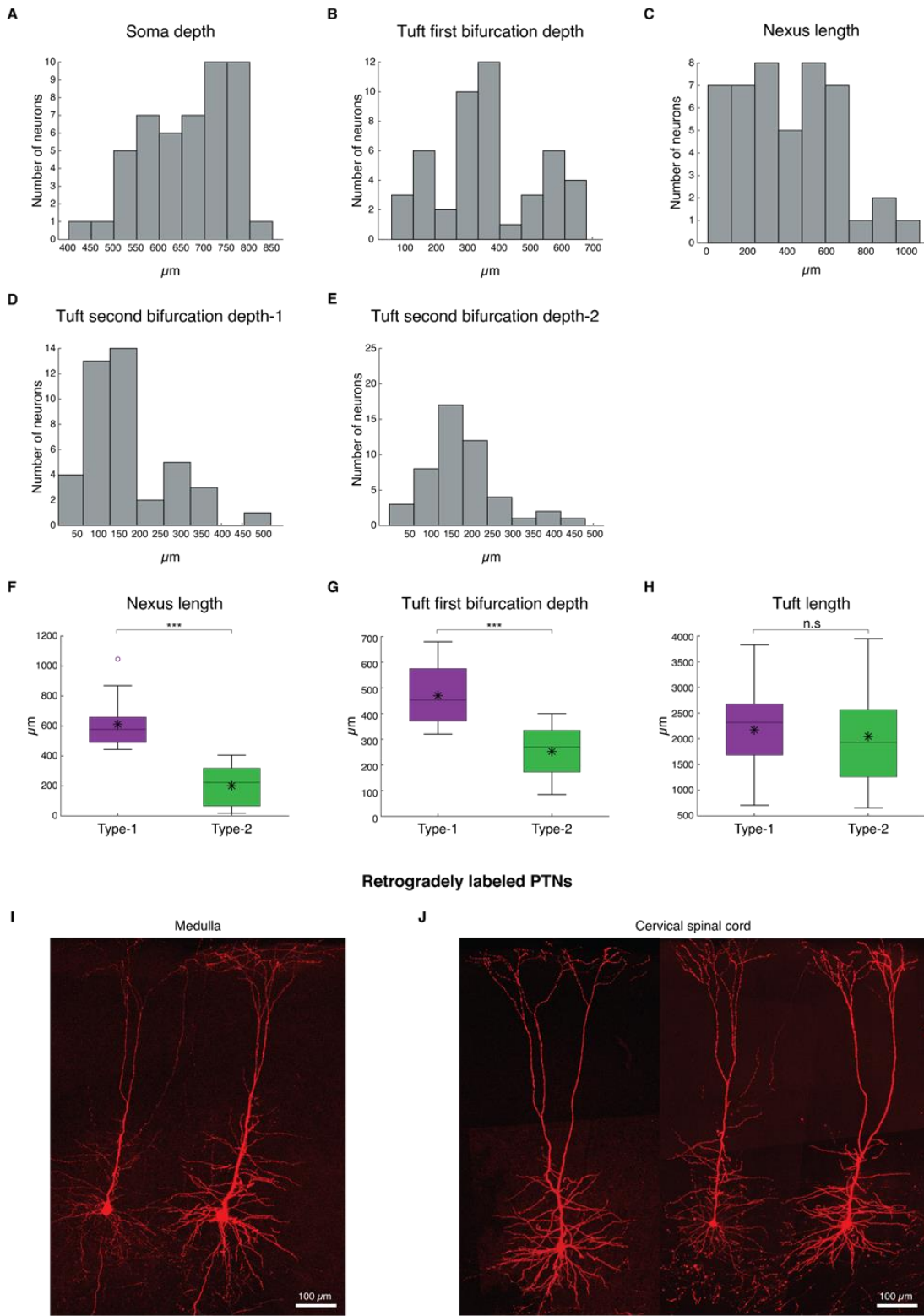
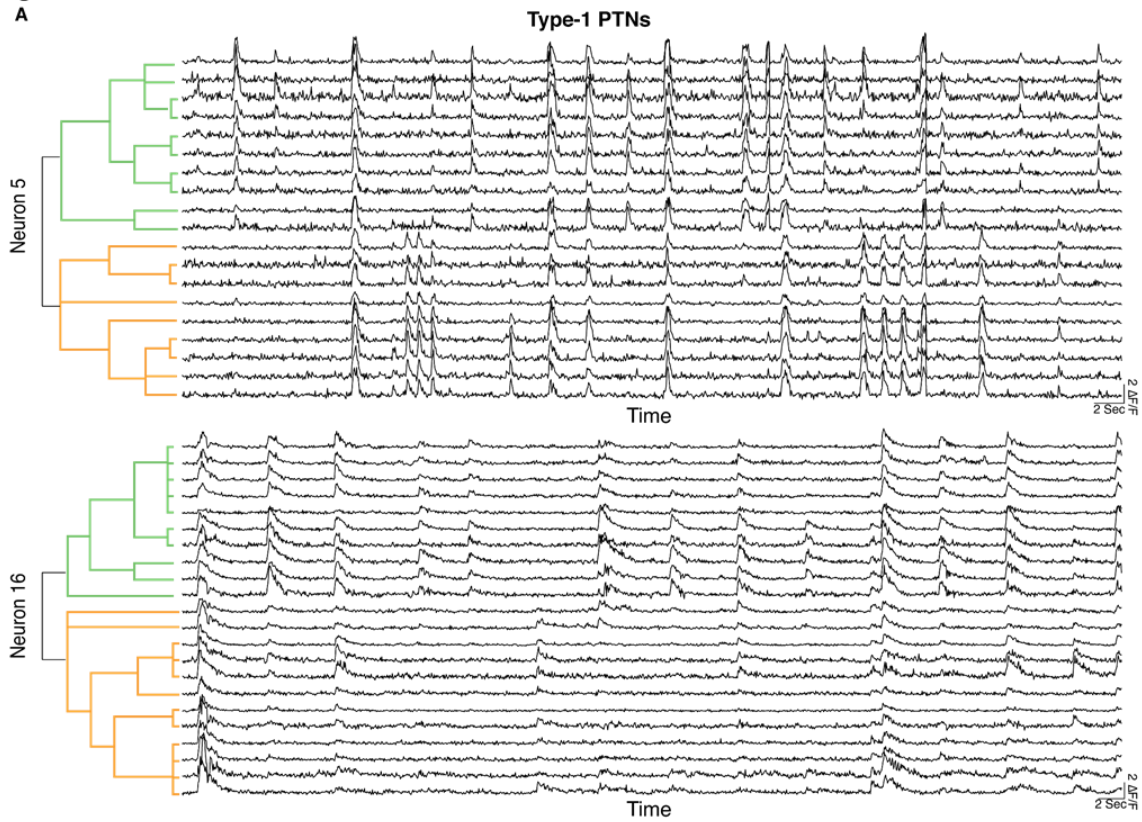


Fig. S1. Anatomical parameters of apical dendrites.

(**A-E**) Histogram of the following parameters (in μm): soma depth from pia (**A**), first bifurcation depth from pia (**B**), nexus length calculated as the summed distance between first and second bifurcations of the two primary tuft branches (**C**), second bifurcation depth from pia, first hemi-tree (**D**), second bifurcation depth from pia, second hemi-tree (**E**). (**F-H**) Box plots of the following parameters: nexus length (**F**), first bifurcation depth from pia (**G**) tuft length calculated as the sum of all tuft branches excluding main apical and nexus (**H**). * $p < 0.05$, ** $p < 0.01$, *** $p < 0.001$, asterisks represent mean value, Wilcoxon rank test. (**I**) Retrogradely labeled PTNs in M1 from medulla. (**J**) As in (**I**) from spinal cord (C2-C3 level).

Fig. S2
A



B

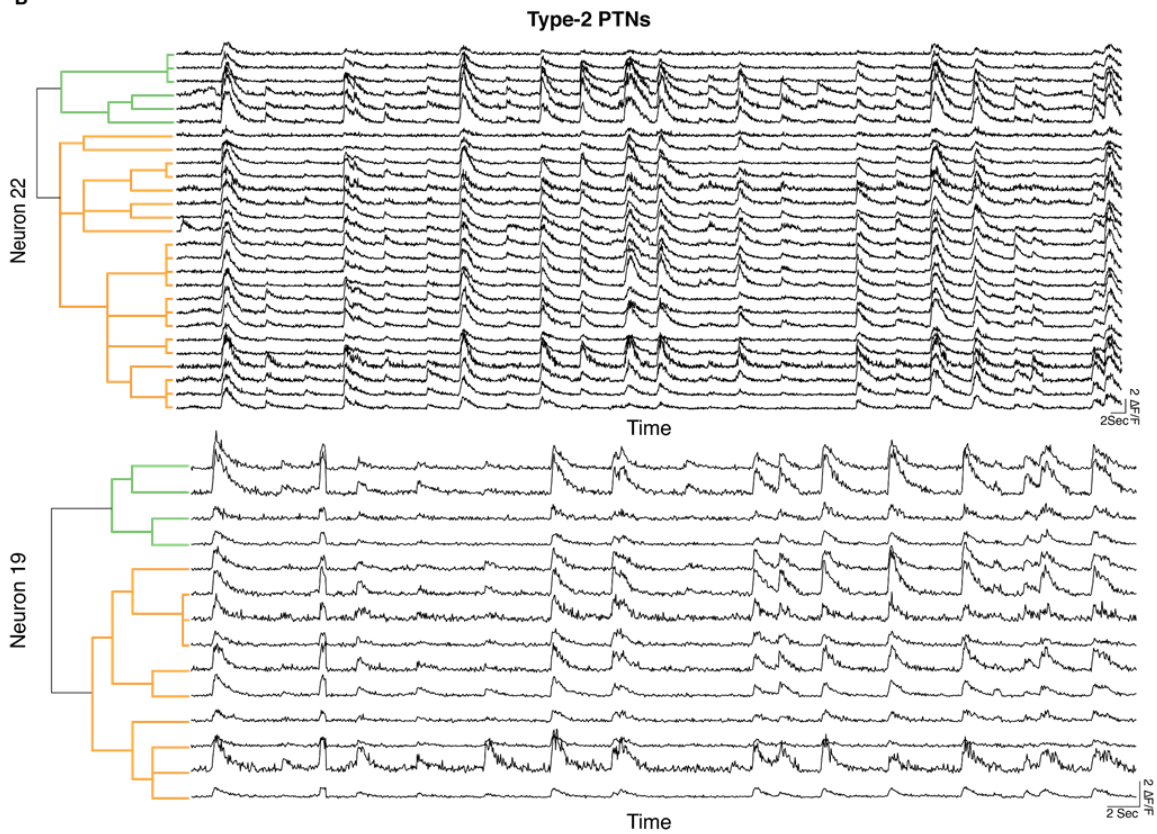


Fig. S2. Example calcium imaging traces for type-1 and type-2 PTNs.

(A) $\Delta F/F$ traces of 2 example type-1 PTNs, same neurons as in Fig. 1H, left. ROIs are arranged by the tree structure as indicated by the dendrogram, left (R, green; L, orange) (B) As in (A) for type-2 PTNs, same neurons as in Fig. 1H, right.

Fig. S3

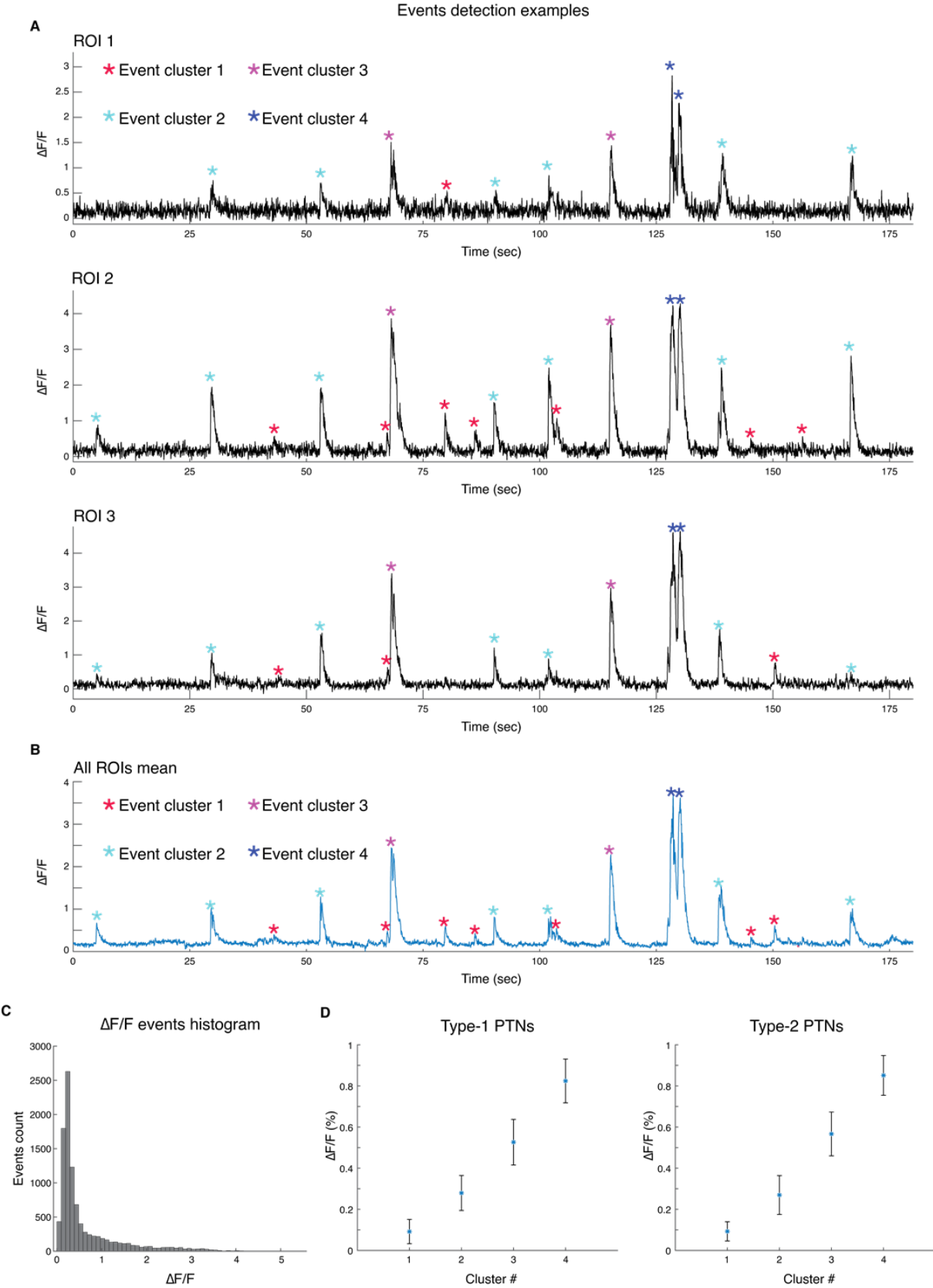


Fig. S3. Calcium events detection.

(A) Example activity ($\Delta F/F$) traces of 3 ROIs from the same tuft tree in a single session. Asterisks represent detected calcium events color coded by event cluster type. (B) Mean activity ($\Delta F/F$) traces across all tuft ROIs sampled from the same neuron in a single session as in (A). (C) calcium events histogram for 21 type-1 and 2 PTNs. PTN (D) The mean (\pm SD) normalized event amplitude per cluster for type-1 (left) and type-2 (right) PTNs.

Fig. S4

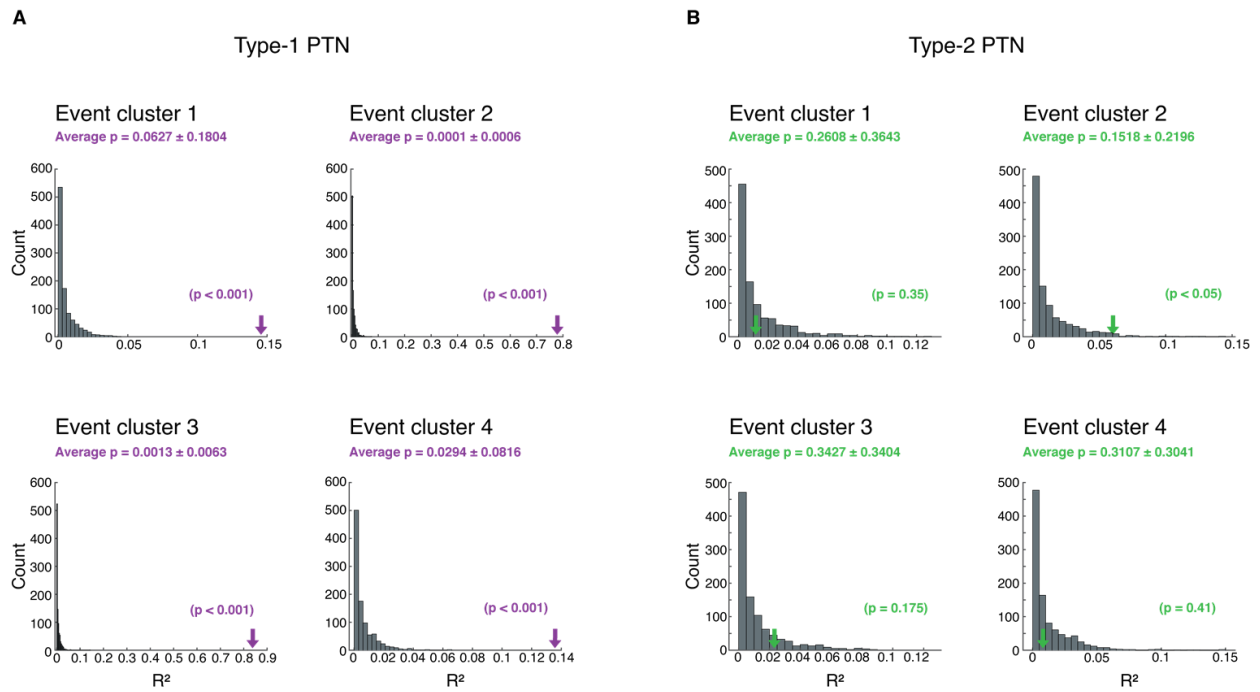


Fig. S4. Shuffling of dendritic distance significantly reduces R^2 of linear regression fit in type-1 but not type-2 PTNs.

(A) Distribution of linear fits of the pair-wise Pearson coefficient per event cluster as a function of shuffled dendritic distances of the ROI pairs (1,000 permutations) for type-1 PTNs. Arrow indicates the experimental R^2 values. P value for the examples are indicated in parentheses and those across experiments (12 neurons, 8 animals, 27 sessions) are indicated in each panel on top

(B) As in (A) for type-2 PTNs (9 neurons, 9 animals, 25 sessions).

Fig. S5

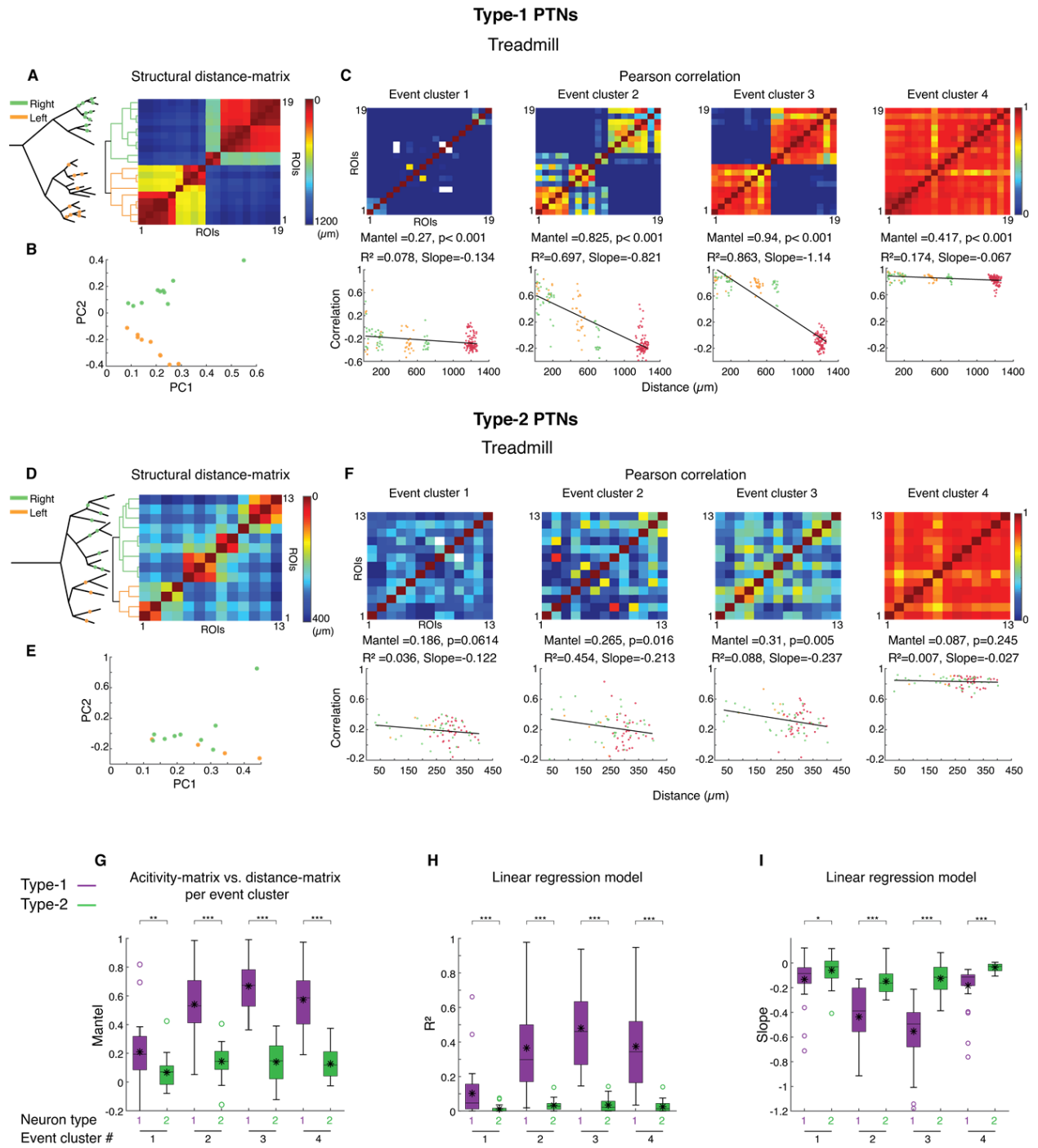


Fig. S5. Pearson's correlation matrices calculated for events clustered by spatial dendritic activation extent.

(A) Left, two-dimensional tree diagram of an example type-1 PTN. Dots represent recorded ROIs. Right, the structural distance-matrix and dendrogram of the same neuron in the left panel. Same example as in Fig. 2C-E. (B) Two-dimensional PCA embedding of all ROIs activity (same neuron as in A), each dot represents a single ROI. (C) Top, matrices showing pairwise Pearson correlation coefficients computed from the calcium signals arranged by the tree structure shown in (A) during the same session as in (B). Bottom, Pearson correlation values as a function of shortest path distance fitted with a linear regression model. (D-F) As in (A-C) for a type-2 PTN during running on treadmill session (same neuron as in Fig. 3A-C). Orange dots, ROIs compared within left hemi-tree; green dots, ROIs compared within right hemi-tree; red dots, ROIs compared between R/L hemi-trees. Black line represents linear regression model fit. (G-I) Box plots of the following parameters: Mantel statistics comparing Pearson correlation and structural distance-matrices (G), R² of linear regression model that predicted Pearson correlations by distance (H), slope of linear regression model that predicted Pearson correlations by distance (I). For all box plots purple represents type-1 and green represents type-2 neurons. * p<0.05, ** p<0.01, *** p<0.001, asterisks represent mean value, Wilcoxon rank test. (Type-1, 12 neurons, 8 animals, 27 sessions; type-2, 9 neurons, 9 animals, 25 sessions).

Fig. S6

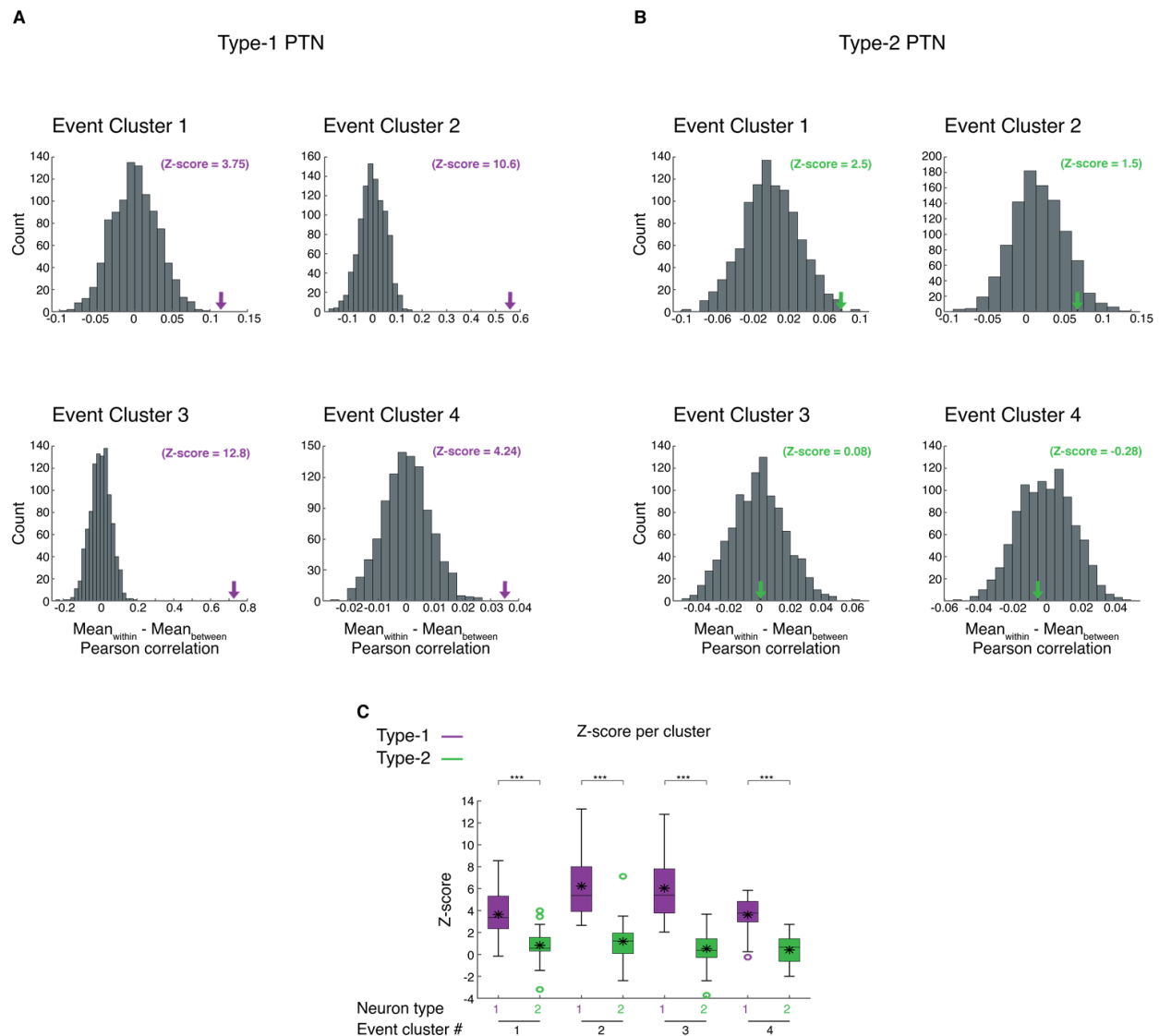


Fig. S6. Shuffling of within and between hemi-tree labels shows significant hemi-tree compartmentalization in type-1 but not type-2 PTNs.

(A) Distribution of $\text{Mean}_{\text{within}} - \text{Mean}_{\text{between}}$ Pearson coefficient of shuffled within and between labels per event cluster (1,000 permutations) for type-1 PTNs. Arrows indicate the experimental value. Z-score value for the example is indicated in parentheses. (B) As in (A) for type-2 PTNs. (C) Box plots of Z-score of the experimental Pearson correlations of within compared to between hemi-trees ($\text{Mean}_{\text{within}} - \text{Mean}_{\text{between}}$) in relation to the shuffled distribution. * $p < 0.05$, ** $p < 0.01$,

*** $p < 0.001$, asterisks represent mean value, Wilcoxon rank test (type-1, 12 neurons, 8 animals, 27 sessions; type-2, 9 neurons, 9 animals, 25 sessions).

Fig. S7

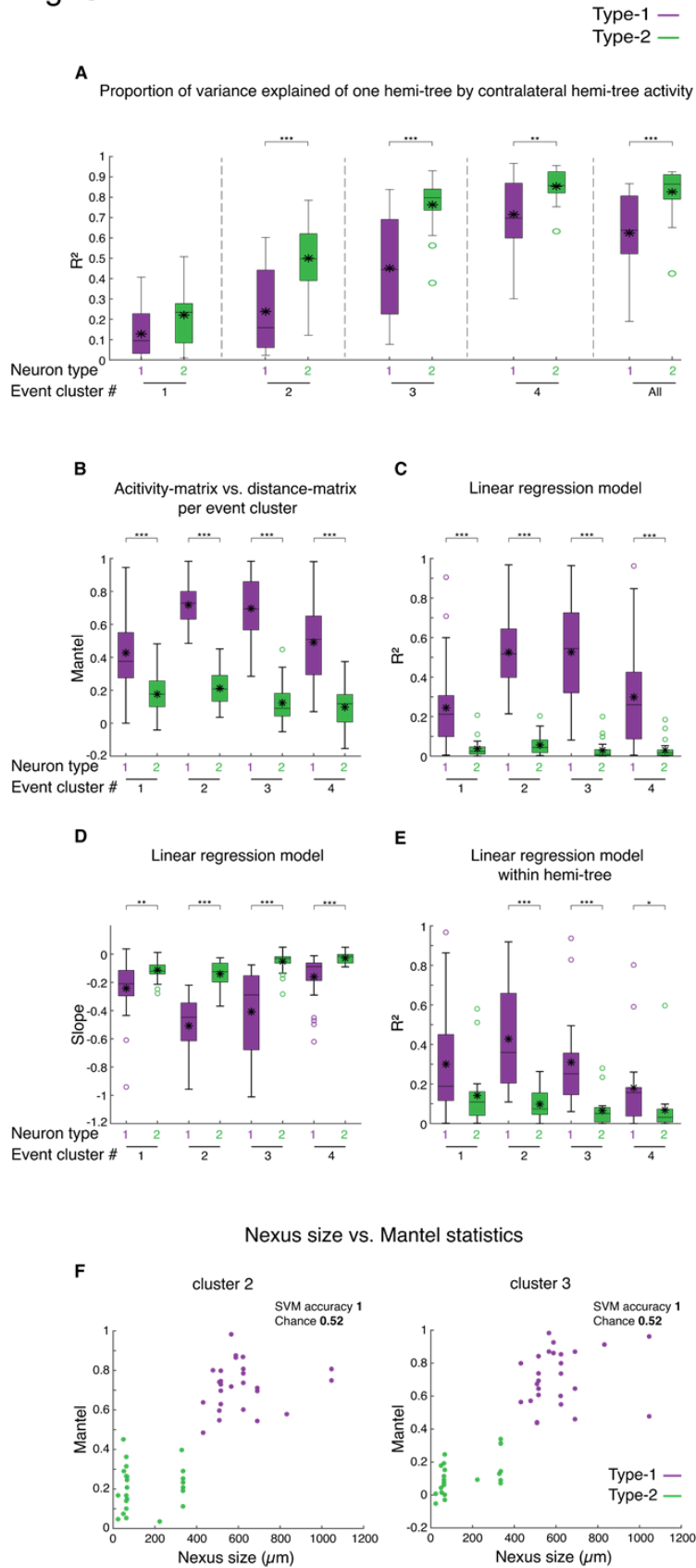


Fig. S7. Statistical comparison between activity of type-1 and type-2 PTNs.

(A) Calculation of the proportion of the variance explained (R^2) of the calcium activity of each ROI in one hemi-tree by the activity of all ROIs in the contralateral hemi-tree using a linear regression model for the four cluster events and the two PTN types. (B-E) Box plots of the following parameters: Mantel statistics for comparison between distance and activity matrices (B), linear regression model R^2 of Pearson correlations as a function of dendritic distance (C), linear regression model slope of Pearson correlations as a function of dendritic distance (D), and linear regression model R^2 of Pearson correlations as a function of dendritic distance within hemi-tree (E). (F) Mantel statistics as a function of nexus size for cluster 2 events (left) and cluster 3 events (right). * $p < 0.05$, ** $p < 0.01$, *** $p < 0.001$, asterisks represent mean value, Wilcoxon rank test. (Type-1, 12 neurons, 8 animals, 27 sessions; type-2, 9 neurons, 9 animals, 25 sessions).

Fig. S8

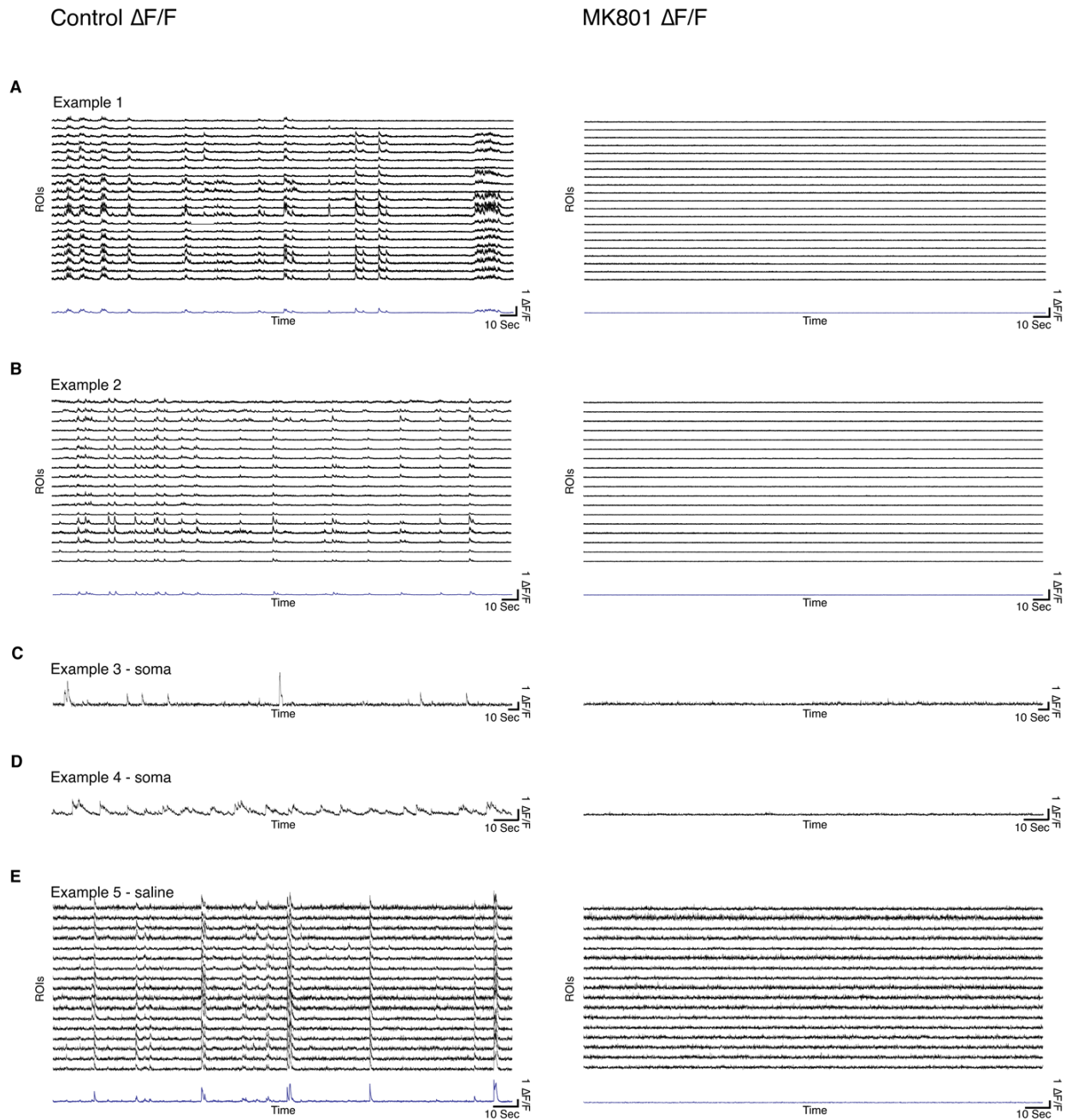


Fig. S8. The NMDAR blocker, MK801, eliminates the calcium activity in tuft dendrites of layer-5 PTNs.

(A) Examples of calcium activity ($\Delta F/F$) traces in different ROIs of the same tuft for a control session (left) and after intracortical injection of MK801 [80 μ M] (right). Blue lower trace shows

the average activity of all ROIs. **(B)** As in (A) for a different neuron. Bottom, mean activity trace across ROIs. **(C-D)** Examples of somatic calcium activity ($\Delta F/F$) for a control session (left) and after intracortical injection of MK801 [80 μM] (right) for two neurons. **(E)** Examples of calcium activity ($\Delta F/F$) traces in different ROIs of the same tuft with intracortical saline injection (left), followed by intracortical injection of MK801 (80 μM) (right).

Fig. S9

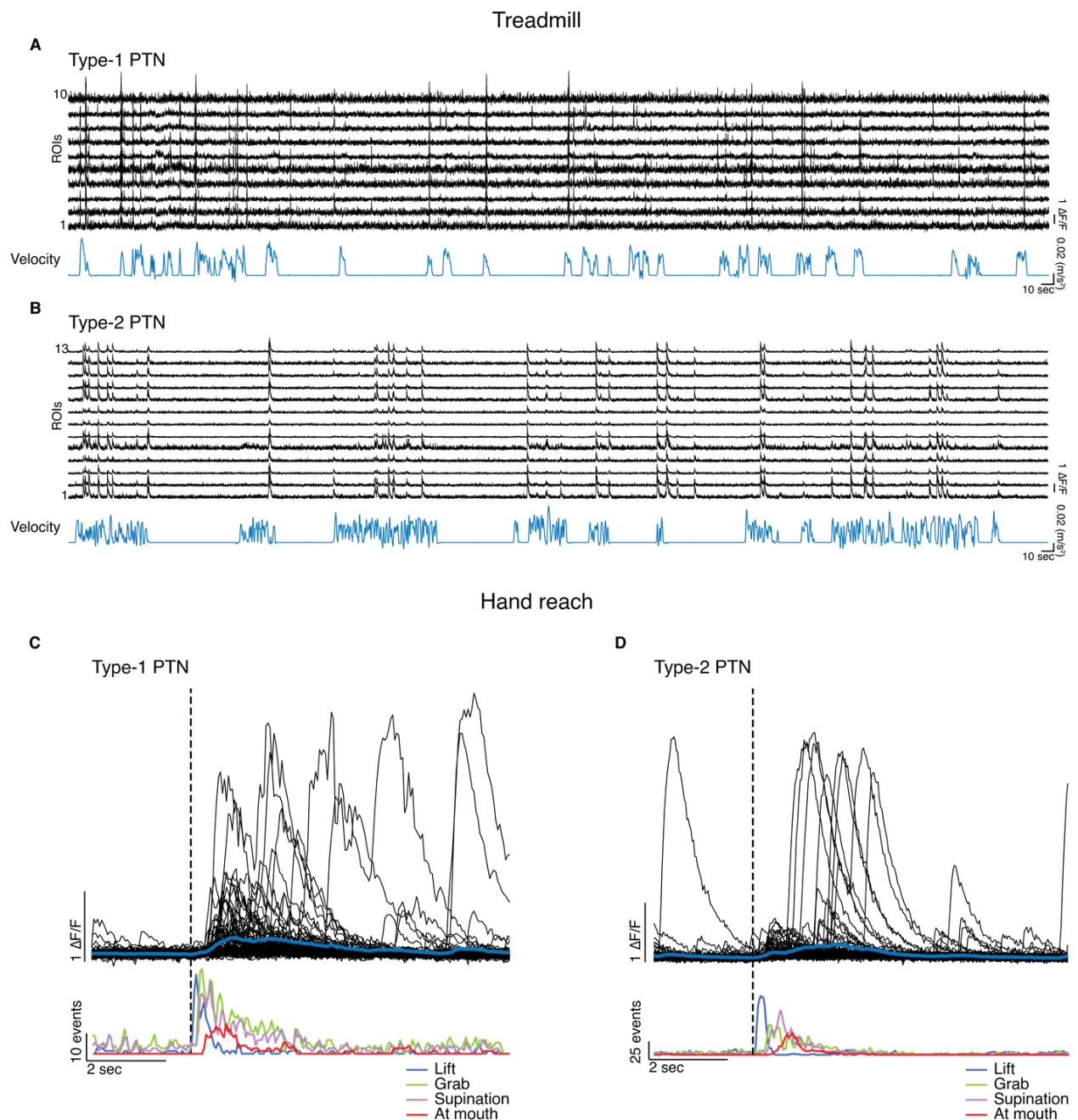


Fig. S9. Calcium activity is correlated to motor behavior in type-1 and 2 PTNs.

(A) Top, $\Delta F/F$ traces from an example type-1 PTN during a running on treadmill session. Bottom, velocity trace. (B) As in (A) for an example type-2 PTN. (C) Top, mean $\Delta F/F$ traces from an example type-1 PTN during a hand reach task session. Each black line represents mean activity

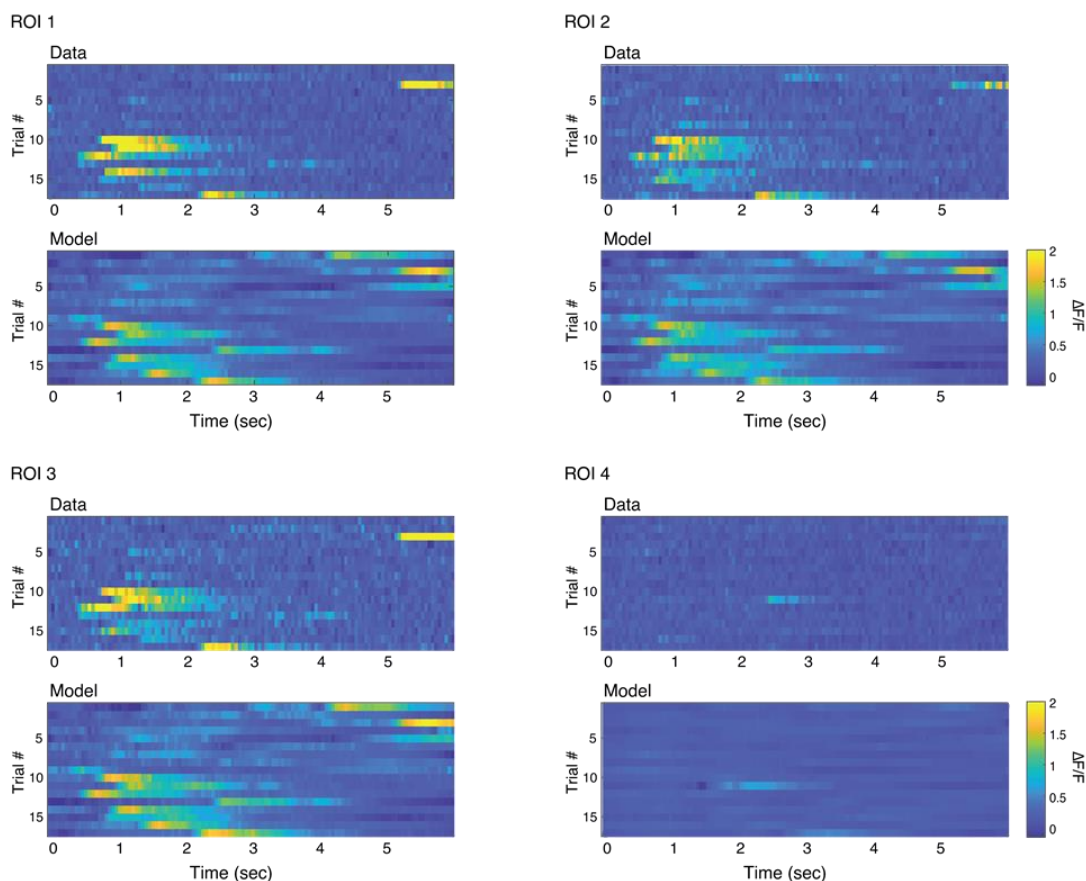
across all ROIs in a single trial. Blue line represents mean activity across ROIs and trials. Bottom, peri-event histogram of the behavioral events over time (sec) from the same behavioral session.

(D) As in (C) for an example type-2 PTN.

Fig. S10

A

GLM model per ROI for an example type-1 PTN



B

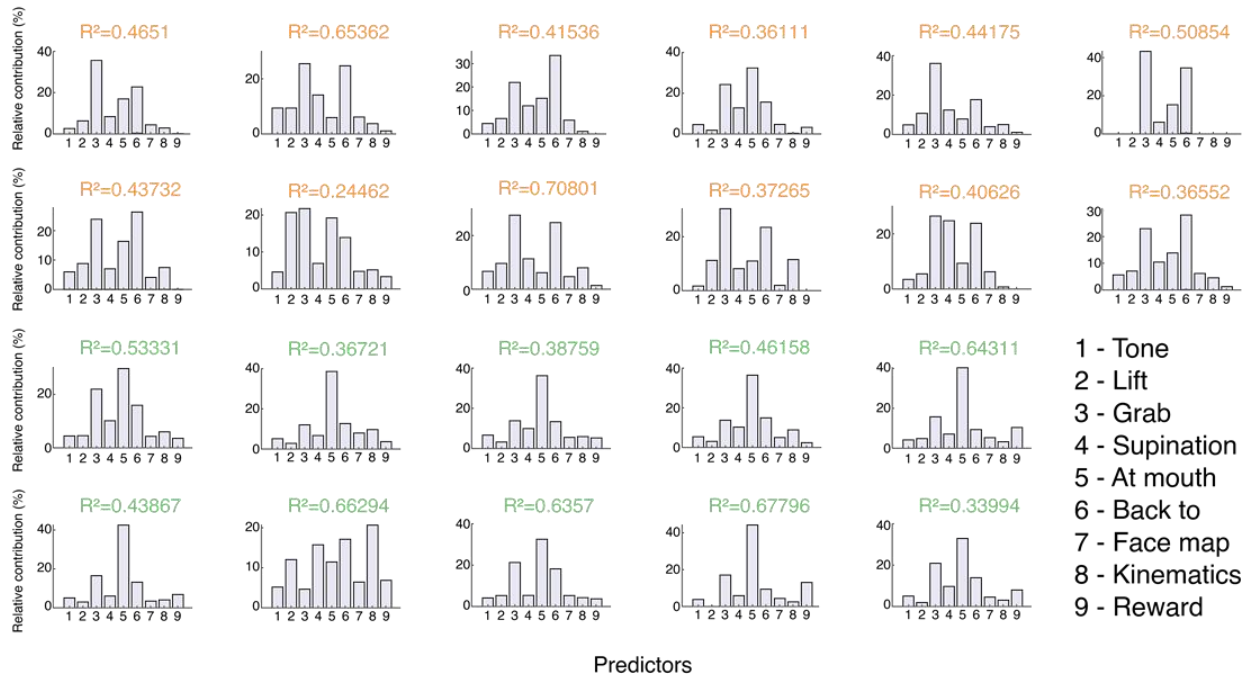


Fig. S10. Examples for GLM model fit and relative contribution of modeled ROIs.

(A) Examples of 4 modeled ROIs from the same neuron in the same session. Top, in vivo recorded data. Bottom, GLM prediction model. (B) The relative contribution for each of the modeled ROIs from the same neuron in a single session as in (A) and in Fig. 5A-E for each of 9 behavioral predictors (see legend) composing the full model. R^2 shown above each graph is the full model value. Color coded by R/L hemi tree (Right, green; left, orange).

Fig. S11

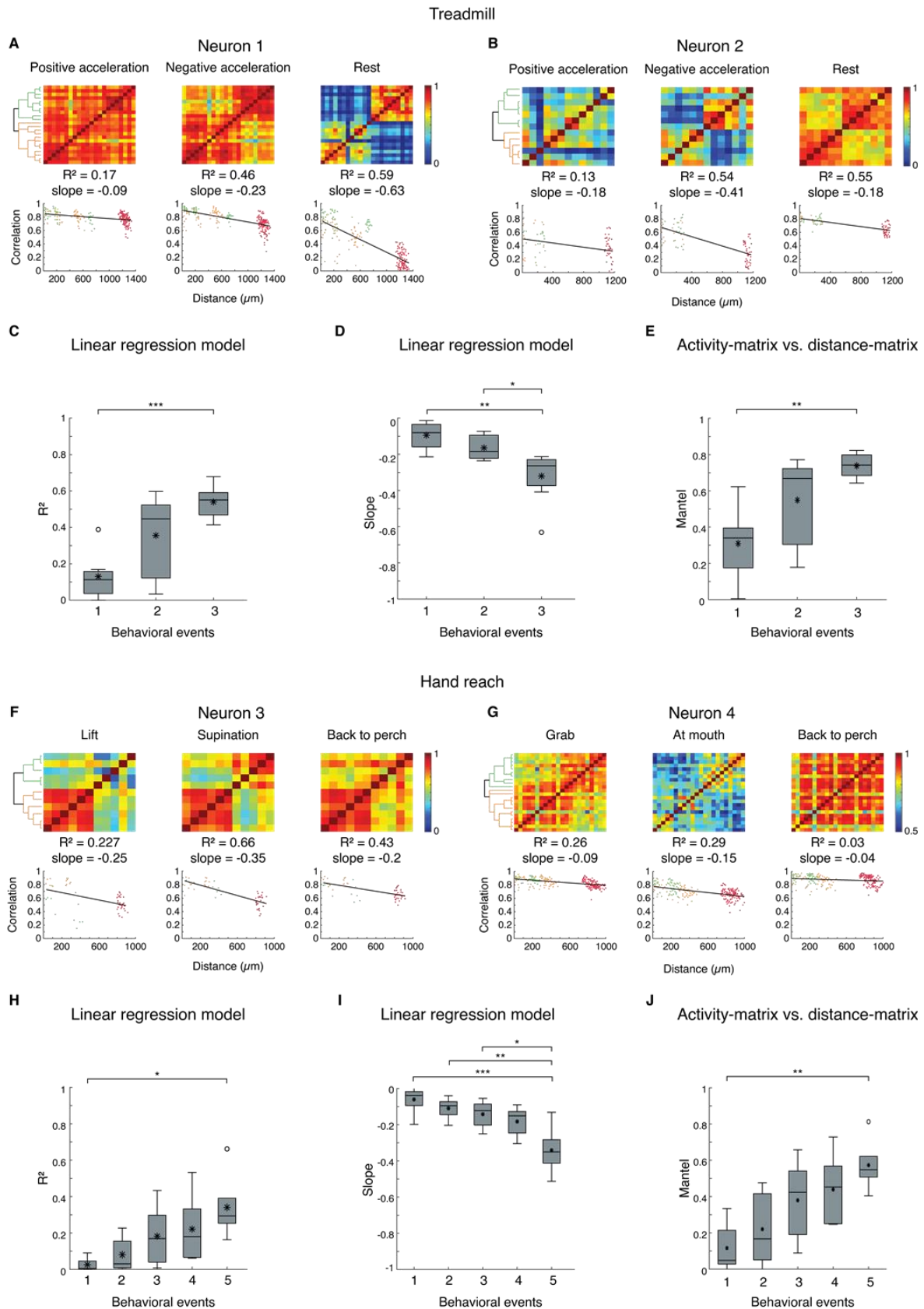


Fig. S11. Peri-behavioral event Pearson correlation matrices for type-1 PTNs. (A) Top, matrices showing pairwise Pearson correlation coefficients computed from the calcium signals that appear during different specific behavioral time windows arranged by the tree structure (shown in left) during a treadmill session. Behavioral events (rest, positive and negative acceleration) are indicated above each panel. Bottom, Pearson correlation values as a function of shortest path distance fitted with a linear regression model. (B) As in (A) for a second neuron example. (C-E) Box plots (arranged by the magnitude) of the following parameters: R² of linear regression model that predicted Pearson correlations by distance (C), slope of linear regression model that predicted Pearson correlations by distance (D), Mantel statistics comparing Pearson correlation and structural distance-matrices (E). To allow averaging between neurons the behavioral events were ranked according to their magnitude. (F-J) as in (A-E) for hand reach task. Behavioral events (lift, grab, supinate, at mouth, back to perch). * p<0.05, **p<0.01, *** p<0.001, blue asterisk, represents mean value for each event cluster. One-way ANOVA with Tukey post-hoc test between event clusters (for treadmill, 6 neurons, 5 animals; for hand reach, 5 neurons, 5 animals).

Fig. S12

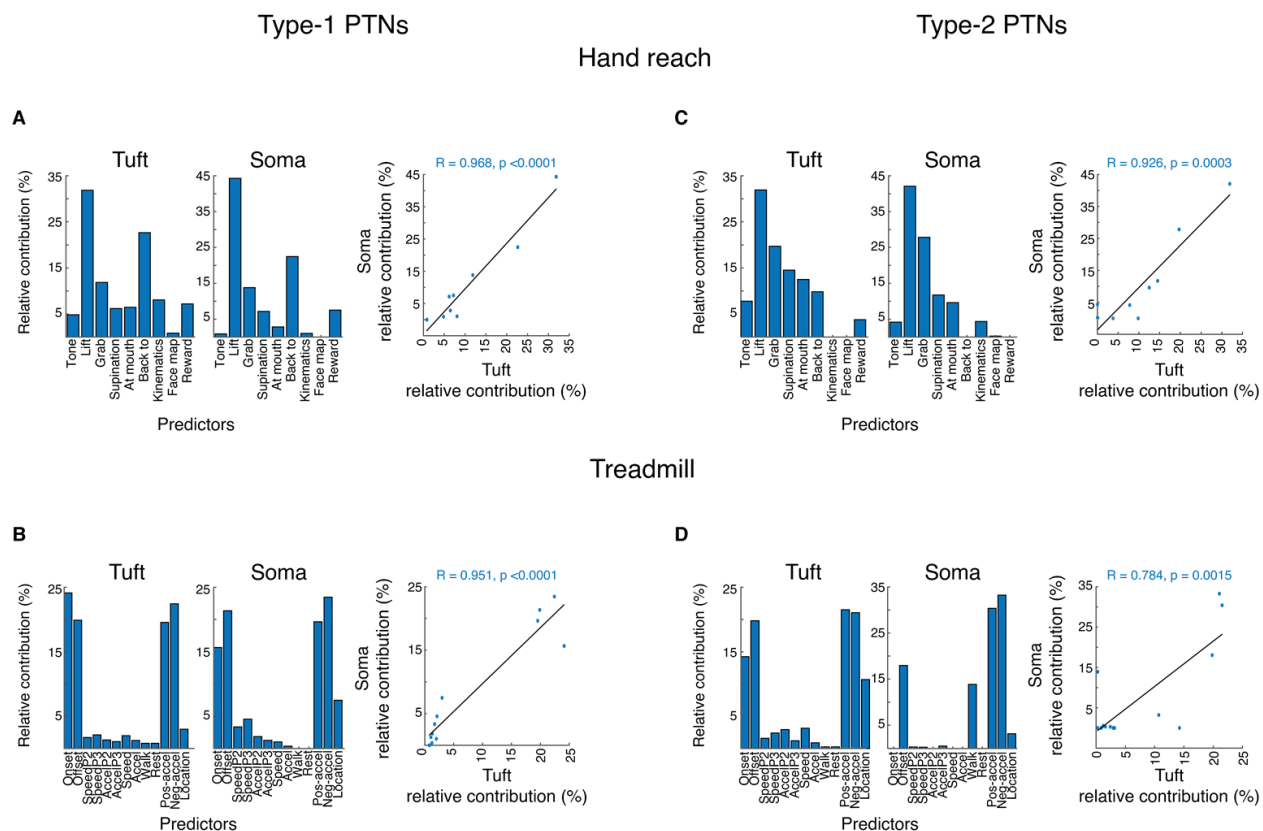


Fig. S12. Correlations between somatic and tuft GLMs modeling the contribution of the behavioral predictors to calcium activity.

(A) The mean relative contribution of the behavioral predictors for all recorded tuft ROIs for a type-1 PTN during hand reach task session (left), and for the corresponding soma (middle). Right, the relative contribution of each behavioral predictor for the soma as a function of the same mean behavioral predictor for the tuft ROIs. Black line represents linear fit model. (B) As in (A) for an example type-1 PTN during running on treadmill session. (C-D) As in (A-B) for an example type-2 PTN.

Fig. S13

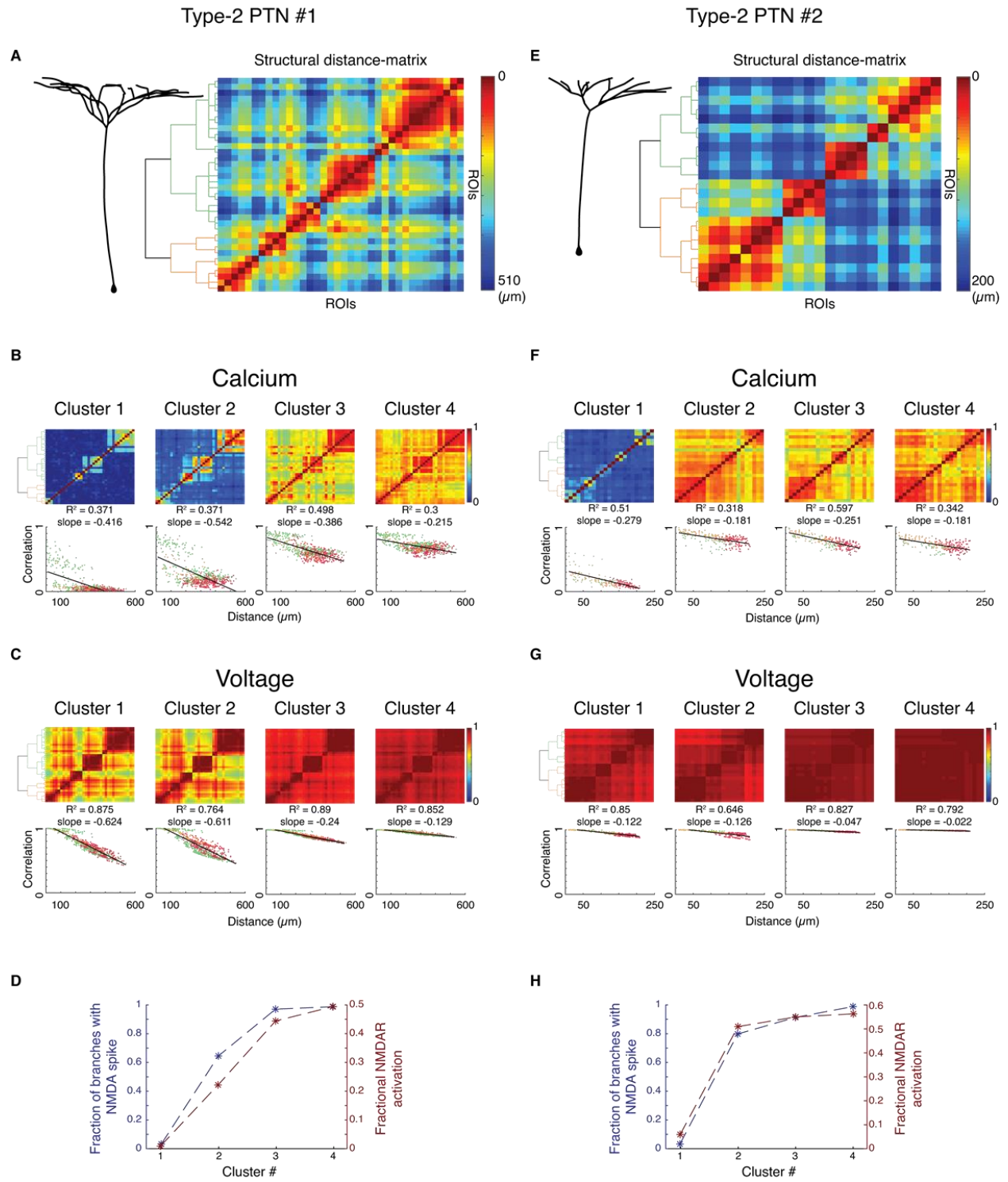


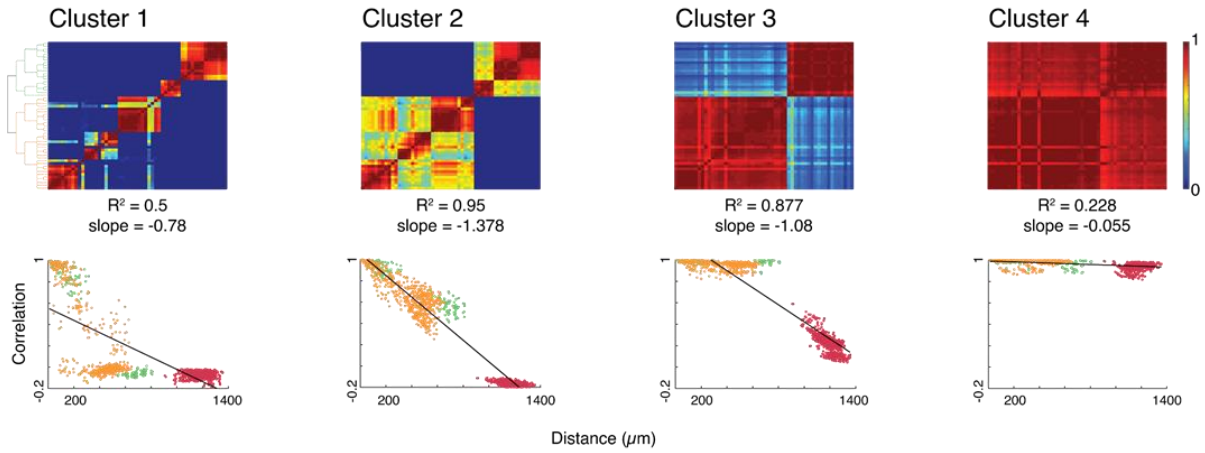
Fig. S13. Correlated tuft tree activity in simulated type-2 PTNs.

(A) Simulation of a type-2 PTN with a relatively large tuft tree (same neuron as in Fig. 3A). Left, side view, right, structural distance-matrix (B) Top, matrices showing pairwise Pearson correlation coefficients computed from the calcium signals arranged by the tree structure as indicated by the dendrogram shown in (A). Bottom, Pearson correlation values as a function of shortest path distance, fitted with a linear regression model. (C) As in (B), for voltage correlations. (D) The percent of tuft dendrites with NMDA-spikes (blue) and the fractional NMDAR conductance (brown) for all event clusters. (E-H) As (A-D) for a second example type-2 PTN with a smaller tuft.

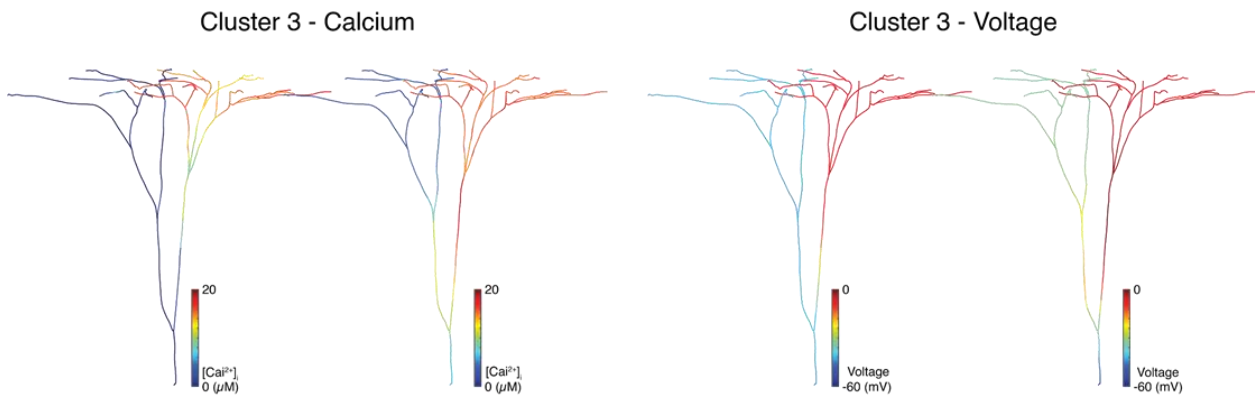
Fig. S14

A

Non-random distance dependent input activation of a type-1 tuft PTN

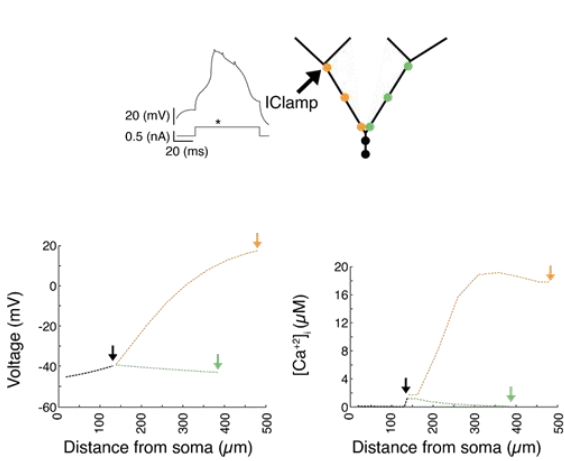


B



C

Calcium spike confined to one hemi-tree



D

Electrically independent hemi-tree

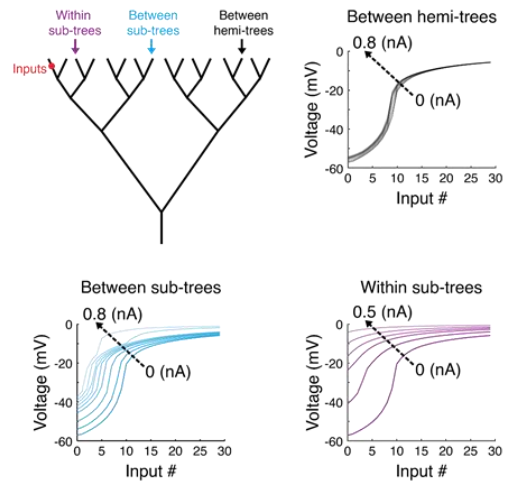


Fig. S14. Modeling the mechanisms of type-1 PTN hemi-tree compartmentalization.

(A) Pearson Correlation matrices between simulated calcium signals on tuft dendrites of a type-1 PTN for each of the event clusters. The tuft was stimulated with synaptic inputs contacting dendrites non randomly favoring contacts in same and neighboring dendrites (see methods). Top, correlation matrix, bottom, Pearson correlation values as a function of shortest path distance fitted with linear regression. (B) Representative examples for changes in the internal calcium (left) and voltage (right). (C) Example of a simulated calcium spike propagation confined to a single hemi-tree. Top, calcium spike was initiated by current injection at a second bifurcation (arrow). The spread of voltage (bottom, left) and calcium (bottom, right) signals was measured along the nexus (green, orange) and the main apical trunk (black) at the time point marked by the asterisk. Arrows on the bottom plot represent the first (black) and the second (green, orange) bifurcations. (D) Voltage and current interactions as a function of dendritic distance. Varying levels of synaptic input conductance (composed of AMPA and NMDA receptors) were activated on a terminal branch marked by the red dot (left) to produce the sigmoidal input-output relation, typical of an NMDA-spike (right). Synaptic input was paired with a current-clamp injection in one of three locations: a neighboring branch within the sub-tree (purple arrow), a terminal dendrite that shared a common second bifurcation (blue arrow), and a tuft branch on the second hemi-tree (black arrow). The current amplitude was increased between trials to create a family of input-output curves for each of the cases (top, right, bottom). Electrical interactions of different degrees were evident between sister branches on the same hemi-tree but were absent between hemi-trees. Simulated neuron for all panels as in Fig. 2C.

References and Notes

1. T. Branco, M. Häusser, The single dendritic branch as a fundamental functional unit in the nervous system. *Curr. Opin. Neurobiol.* **20**, 494–502 (2010). [doi:10.1016/j.conb.2010.07.009](https://doi.org/10.1016/j.conb.2010.07.009) [Medline](#)
2. X. E. Wu, B. W. Mel, Capacity-enhancing synaptic learning rules in a medial temporal lobe online learning model. *Neuron* **62**, 31–41 (2009). [doi:10.1016/j.neuron.2009.02.021](https://doi.org/10.1016/j.neuron.2009.02.021) [Medline](#)
3. G. J. Stuart, N. Spruston, Dendritic integration: 60 years of progress. *Nat. Neurosci.* **18**, 1713–1721 (2015). [doi:10.1038/nn.4157](https://doi.org/10.1038/nn.4157) [Medline](#)
4. G. Major, M. E. Larkum, J. Schiller, Active properties of neocortical pyramidal neuron dendrites. *Annu. Rev. Neurosci.* **36**, 1–24 (2013). [doi:10.1146/annurev-neuro-062111-150343](https://doi.org/10.1146/annurev-neuro-062111-150343) [Medline](#)
5. S. D. Antic, W. L. Zhou, A. R. Moore, S. M. Short, K. D. Ikonomu, The decade of the dendritic NMDA spike. *J. Neurosci. Res.* **88**, 2991–3001 (2010). [doi:10.1002/jnr.22444](https://doi.org/10.1002/jnr.22444) [Medline](#)
6. J. Cichon, W. B. Gan, Branch-specific dendritic Ca(2+) spikes cause persistent synaptic plasticity. *Nature* **520**, 180–185 (2015). [doi:10.1038/nature14251](https://doi.org/10.1038/nature14251) [Medline](#)
7. L. M. Palmer, A. S. Shai, J. E. Reeve, H. L. Anderson, O. Paulsen, M. E. Larkum, NMDA spikes enhance action potential generation during sensory input. *Nat. Neurosci.* **17**, 383–390 (2014). [doi:10.1038/nn.3646](https://doi.org/10.1038/nn.3646) [Medline](#)
8. L. Beaulieu-Laroche, E. H. S. Toloza, N. J. Brown, M. T. Harnett, Widespread and Highly Correlated Somato-dendritic Activity in Cortical Layer 5 Neurons. *Neuron* **103**, 235–241.e4 (2019). [doi:10.1016/j.neuron.2019.05.014](https://doi.org/10.1016/j.neuron.2019.05.014) [Medline](#)
9. V. Francioni, Z. Padamsey, N. L. Rochefort, High and asymmetric somato-dendritic coupling of V1 layer 5 neurons independent of visual stimulation and locomotion. *eLife* **8**, e49145 (2019). [doi:10.7554/eLife.49145](https://doi.org/10.7554/eLife.49145) [Medline](#)
10. J. Voigts, M. T. Harnett, Somatic and Dendritic Encoding of Spatial Variables in Retrosplenial Cortex Differs during 2D Navigation. *Neuron* **105**, 237–245.e4 (2020). [doi:10.1016/j.neuron.2019.10.016](https://doi.org/10.1016/j.neuron.2019.10.016) [Medline](#)
11. A. Kerlin, B. Mohar, D. Flickinger, B. J. MacLennan, M. B. Dean, C. Davis, N. Spruston, K. Svoboda, Functional clustering of dendritic activity during decision-making. *eLife* **8**, e46966 (2019). [doi:10.7554/eLife.46966](https://doi.org/10.7554/eLife.46966) [Medline](#)
12. N. L. Xu, M. T. Harnett, S. R. Williams, D. Huber, D. H. O'Connor, K. Svoboda, J. C. Magee, Nonlinear dendritic integration of sensory and motor input during an active sensing task. *Nature* **492**, 247–251 (2012). [doi:10.1038/nature11601](https://doi.org/10.1038/nature11601) [Medline](#)
13. C. O. Lacefield, E. A. Pnevmatikakis, L. Paninski, R. M. Bruno, Reinforcement Learning Recruits Somata and Apical Dendrites across Layers of Primary Sensory Cortex. *Cell Rep.* **26**, 2000–2008.e2 (2019). [doi:10.1016/j.celrep.2019.01.093](https://doi.org/10.1016/j.celrep.2019.01.093) [Medline](#)

14. B. B. Ujfalussy, J. K. Makara, M. Lengyel, T. Branco, Global and Multiplexed Dendritic Computations under In Vivo-like Conditions. *Neuron* **100**, 579–592.e5 (2018). [doi:10.1016/j.neuron.2018.08.032](https://doi.org/10.1016/j.neuron.2018.08.032) [Medline](#)
15. R. Naud, B. Bathellier, W. Gerstner, Spike-timing prediction in cortical neurons with active dendrites. *Front. Comput. Neurosci.* **8**, 90 (2014). [doi:10.3389/fncom.2014.00090](https://doi.org/10.3389/fncom.2014.00090) [Medline](#)
16. P. Poirazi, T. Brannon, B. W. Mel, Pyramidal neuron as two-layer neural network. *Neuron* **37**, 989–999 (2003). [doi:10.1016/S0896-6273\(03\)00149-1](https://doi.org/10.1016/S0896-6273(03)00149-1) [Medline](#)
17. D. Beniaguev, I. Segev, M. London, Single cortical neurons as deep artificial neural networks. *Neuron* **109**, 2727–2739.e3 (2021). [doi:10.1016/j.neuron.2021.07.002](https://doi.org/10.1016/j.neuron.2021.07.002) [Medline](#)
18. A. Payeur, J. C. Béïque, R. Naud, Classes of dendritic information processing. *Curr. Opin. Neurobiol.* **58**, 78–85 (2019). [doi:10.1016/j.conb.2019.07.006](https://doi.org/10.1016/j.conb.2019.07.006) [Medline](#)
19. G. Kastellakis, P. Poirazi, Synaptic Clustering and Memory Formation. *Front. Mol. Neurosci.* **12**, 300 (2019). [doi:10.3389/fnmol.2019.00300](https://doi.org/10.3389/fnmol.2019.00300) [Medline](#)
20. R. Legenstein, W. Maass, Branch-specific plasticity enables self-organization of nonlinear computation in single neurons. *J. Neurosci.* **31**, 10787–10802 (2011). [doi:10.1523/JNEUROSCI.5684-10.2011](https://doi.org/10.1523/JNEUROSCI.5684-10.2011) [Medline](#)
21. J. Bono, C. Clopath, Modeling somatic and dendritic spike mediated plasticity at the single neuron and network level. *Nat. Commun.* **8**, 706 (2017). [doi:10.1038/s41467-017-00740-z](https://doi.org/10.1038/s41467-017-00740-z) [Medline](#)
22. B. W. Mel, in *Advances in Neural Information Processing Systems*, J. Moody, S. Hanson, R. Lippmann, Eds. (Morgan Kaufmann, 1992), vol. 4, pp. 35–42.
23. M. N. Economo, S. Viswanathan, B. Tasic, E. Bas, J. Winnubst, V. Menon, L. T. Graybiel, T. N. Nguyen, K. A. Smith, Z. Yao, L. Wang, C. R. Gerfen, J. Chandrashekar, H. Zeng, L. L. Looger, K. Svoboda, Distinct descending motor cortex pathways and their roles in movement. *Nature* **563**, 79–84 (2018). [doi:10.1038/s41586-018-0642-9](https://doi.org/10.1038/s41586-018-0642-9) [Medline](#)
24. H. Markram, E. Muller, S. Ramaswamy, M. W. Reimann, M. Abdellah, C. A. Sanchez, A. Ailamaki, L. Alonso-Nanclares, N. Antille, S. Arsever, G. A. A. Kahou, T. K. Berger, A. Bilgili, N. Buncic, A. Chalimourda, G. Chindemi, J.-D. Courcol, F. Delalondre, V. Delattre, S. Druckmann, R. Dumusc, J. Dynes, S. Eilemann, E. Gal, M. E. Gevaert, J.-P. Ghobril, A. Gidon, J. W. Graham, A. Gupta, V. Haenel, E. Hay, T. Heinis, J. B. Hernando, M. Hines, L. Kanari, D. Keller, J. Kenyon, G. Khazen, Y. Kim, J. G. King, Z. Kisvarday, P. Kumbhar, S. Lasserre, J.-V. Le Bé, B. R. C. Magalhães, A. Merchán-Pérez, J. Meystre, B. R. Morrice, J. Muller, A. Muñoz-Céspedes, S. Muralidhar, K. Muthurasa, D. Nachbaur, T. H. Newton, M. Nolte, A. Ovcharenko, J. Palacios, L. Pastor, R. Perin, R. Ranjan, I. Riachi, J.-R. Rodríguez, J. L. Riquelme, C. Rössert, K. Sfyarakis, Y. Shi, J. C. Shillcock, G. Silberberg, R. Silva, F. Tauheed, M. Telefont, M. Toledo-Rodriguez, T. Tränkler, W. Van Geit, J. V. Díaz, R. Walker, Y. Wang, S. M. Zaninetta, J. DeFelipe, S. L. Hill, I. Segev, F. Schürmann, Reconstruction and Simu. *Cell* **163**, 456–492 (2015). [doi:10.1016/j.cell.2015.09.029](https://doi.org/10.1016/j.cell.2015.09.029) [Medline](#)

25. W. J. Gao, Z. H. Zheng, Target-specific differences in somatodendritic morphology of layer V pyramidal neurons in rat motor cortex. *J. Comp. Neurol.* **476**, 174–185 (2004). [doi:10.1002/cne.20224](https://doi.org/10.1002/cne.20224) [Medline](#)
26. Y. Wang, M. Ye, X. Kuang, Y. Li, S. Hu, A simplified morphological classification scheme for pyramidal cells in six layers of primary somatosensory cortex of juvenile rats. *IBRO Rep.* **5**, 74–90 (2018). [doi:10.1016/j.ibror.2018.10.001](https://doi.org/10.1016/j.ibror.2018.10.001) [Medline](#)
27. S. Jiang, Y. Guan, S. Chen, X. Jia, H. Ni, Y. Zhang, Y. Han, X. Peng, C. Zhou, A. Li, Q. Luo, H. Gong, Anatomically revealed morphological patterns of pyramidal neurons in layer 5 of the motor cortex. *Sci. Rep.* **10**, 7916 (2020). [doi:10.1038/s41598-020-64665-2](https://doi.org/10.1038/s41598-020-64665-2) [Medline](#)
28. G. M. Shepherd, Corticostriatal connectivity and its role in disease. *Nat. Rev. Neurosci.* **14**, 278–291 (2013). [doi:10.1038/nrn3469](https://doi.org/10.1038/nrn3469) [Medline](#)
29. A. Groh, H. S. Meyer, E. F. Schmidt, N. Heintz, B. Sakmann, P. Krieger, Cell-type specific properties of pyramidal neurons in neocortex underlying a layout that is modifiable depending on the cortical area. *Cereb. Cortex* **20**, 826–836 (2010). [doi:10.1093/cercor/bhp152](https://doi.org/10.1093/cercor/bhp152) [Medline](#)
30. E. J. Kim, A. L. Juavinett, E. M. Kyubwa, M. W. Jacobs, E. M. Callaway, Three Types of Cortical Layer 5 Neurons That Differ in Brain-wide Connectivity and Function. *Neuron* **88**, 1253–1267 (2015). [doi:10.1016/j.neuron.2015.11.002](https://doi.org/10.1016/j.neuron.2015.11.002) [Medline](#)
31. A. M. Hattox, S. B. Nelson, Layer V neurons in mouse cortex projecting to different targets have distinct physiological properties. *J. Neurophysiol.* **98**, 3330–3340 (2007). [doi:10.1152/jn.00397.2007](https://doi.org/10.1152/jn.00397.2007) [Medline](#)
32. B. Tasic, Z. Yao, L. T. Graybiel, K. A. Smith, T. N. Nguyen, D. Bertagnolli, J. Goldy, E. Garren, M. N. Economo, S. Viswanathan, O. Penn, T. Bakken, V. Menon, J. Miller, O. Fong, K. E. Hirokawa, K. Lathia, C. Rimorin, M. Tieu, R. Larsen, T. Casper, E. Barkan, M. Kroll, S. Parry, N. V. Shapovalova, D. Hirschstein, J. Pendergraft, H. A. Sullivan, T. K. Kim, A. Szafer, N. Dee, P. Groblewski, I. Wickersham, A. Cetin, J. A. Harris, B. P. Levi, S. M. Sunkin, L. Madisen, T. L. Daigle, L. Looger, A. Bernard, J. Phillips, E. Lein, M. Hawrylycz, K. Svoboda, A. R. Jones, C. Koch, H. Zeng, Shared and distinct transcriptomic cell types across neocortical areas. *Nature* **563**, 72–78 (2018). [doi:10.1038/s41586-018-0654-5](https://doi.org/10.1038/s41586-018-0654-5) [Medline](#)
33. L. N. Fletcher, S. R. Williams, Neocortical Topology Governs the Dendritic Integrative Capacity of Layer 5 Pyramidal Neurons. *Neuron* **101**, 76–90.e4 (2019). [doi:10.1016/j.neuron.2018.10.048](https://doi.org/10.1016/j.neuron.2018.10.048) [Medline](#)
34. S. Levy, M. Lavzin, H. Benisty, A. Ghanayim, U. Dubin, S. Achvat, Z. Brosh, F. Aeed, B. D. Mensh, Y. Schiller, R. Meir, O. Barak, R. Talmon, A. W. Hantman, J. Schiller, Cell-Type-Specific Outcome Representation in the Primary Motor Cortex. *Neuron* **107**, 954–971.e9 (2020). [doi:10.1016/j.neuron.2020.06.006](https://doi.org/10.1016/j.neuron.2020.06.006) [Medline](#)
35. F. Fuhrmann, D. Justus, L. Sosulina, H. Kaneko, T. Beutel, D. Friedrichs, S. Schoch, M. K. Schwarz, M. Fuhrmann, S. Remy, Locomotion, Theta Oscillations, and the Speed-Correlated Firing of Hippocampal Neurons Are Controlled by a Medial Septal

- Glutamatergic Circuit. *Neuron* **86**, 1253–1264 (2015). [doi:10.1016/j.neuron.2015.05.001](https://doi.org/10.1016/j.neuron.2015.05.001) [Medline](#)
36. T. W. Chen, T. J. Wardill, Y. Sun, S. R. Pulver, S. L. Renninger, A. Baohan, E. R. Schreiter, R. A. Kerr, M. B. Orger, V. Jayaraman, L. L. Looger, K. Svoboda, D. S. Kim, Ultrasensitive fluorescent proteins for imaging neuronal activity. *Nature* **499**, 295–300 (2013). [doi:10.1038/nature12354](https://doi.org/10.1038/nature12354) [Medline](#)
 37. T. Deneux, A. Kaszas, G. Szalay, G. Katona, T. Lakner, A. Grinvald, B. Rózsa, I. Vanzetta, Accurate spike estimation from noisy calcium signals for ultrafast three-dimensional imaging of large neuronal populations in vivo. *Nat. Commun.* **7**, 12190 (2016). [doi:10.1038/ncomms12190](https://doi.org/10.1038/ncomms12190) [Medline](#)
 38. N. Mantel, The detection of disease clustering and a generalized regression approach. *Cancer Res.* **27**, 209–220 (1967). [Medline](#)
 39. B. Manly, *The Statistics of Natural Selection* (Chapman & Hall, 1985).
 40. P. W. Mielke, Clarification and Appropriate Inferences for Mantel and Valand's Nonparametric Multivariate Analysis Technique. *Biometrics* **34**, 277 (1978). [doi:10.2307/2530017](https://doi.org/10.2307/2530017)
 41. B. Engelhard, J. Finkelstein, J. Cox, W. Fleming, H. J. Jang, S. Ornelas, S. A. Koay, S. Y. Thiberge, N. D. Daw, D. W. Tank, I. B. Witten, Specialized coding of sensory, motor and cognitive variables in VTA dopamine neurons. *Nature* **570**, 509–513 (2019). [doi:10.1038/s41586-019-1261-9](https://doi.org/10.1038/s41586-019-1261-9) [Medline](#)
 42. P. Ramkumar, B. Dekleva, S. Cooler, L. Miller, K. Kording, Premotor and Motor Cortices Encode Reward. *PLOS ONE* **11**, e0160851 (2016). [doi:10.1371/journal.pone.0160851](https://doi.org/10.1371/journal.pone.0160851) [Medline](#)
 43. B. A. Sauerbrei, J.-Z. Guo, J. D. Cohen, M. Mischiati, W. Guo, M. Kabra, N. Verma, B. Mensh, K. Branson, A. W. Hantman, Cortical pattern generation during dexterous movement is input-driven. *Nature* **577**, 386–391 (2020). [doi:10.1038/s41586-019-1869-9](https://doi.org/10.1038/s41586-019-1869-9) [Medline](#)
 44. A. Nashef, O. Cohen, R. Harel, Z. Israel, Y. Prut, Reversible Block of Cerebellar Outflow Reveals Cortical Circuitry for Motor Coordination. *Cell Rep.* **27**, 2608–2619.e4 (2019). [doi:10.1016/j.celrep.2019.04.100](https://doi.org/10.1016/j.celrep.2019.04.100) [Medline](#)
 45. M. Lavzin, S. Rapoport, A. Polsky, L. Garion, J. Schiller, Nonlinear dendritic processing determines angular tuning of barrel cortex neurons in vivo. *Nature* **490**, 397–401 (2012). [doi:10.1038/nature11451](https://doi.org/10.1038/nature11451) [Medline](#)
 46. M. E. Larkum, T. Nevian, M. Sandler, A. Polsky, J. Schiller, Synaptic integration in tuft dendrites of layer 5 pyramidal neurons: A new unifying principle. *Science* **325**, 756–760 (2009). [doi:10.1126/science.1171958](https://doi.org/10.1126/science.1171958) [Medline](#)
 47. M. Larkum, A cellular mechanism for cortical associations: An organizing principle for the cerebral cortex. *Trends Neurosci.* **36**, 141–151 (2013). [doi:10.1016/j.tins.2012.11.006](https://doi.org/10.1016/j.tins.2012.11.006) [Medline](#)

48. H. Jia, N. L. Rochefort, X. Chen, A. Konnerth, Dendritic organization of sensory input to cortical neurons in vivo. *Nature* **464**, 1307–1312 (2010). [doi:10.1038/nature08947](https://doi.org/10.1038/nature08947) [Medline](#)
49. M. E. Sheffield, D. A. Dombeck, Calcium transient prevalence across the dendritic arbour predicts place field properties. *Nature* **517**, 200–204 (2015). [doi:10.1038/nature13871](https://doi.org/10.1038/nature13871) [Medline](#)
50. L. Beaulieu-Laroche, E. H. S. Toloza, M. S. van der Goes, M. Lafourcade, D. Barnagian, Z. M. Williams, E. N. Eskandar, M. P. Frosch, S. S. Cash, M. T. Harnett, Enhanced dendritic compartmentalization in human cortical neurons. *Cell* **175**, 643–651.e14 (2018). [doi:10.1016/j.cell.2018.08.045](https://doi.org/10.1016/j.cell.2018.08.045) [Medline](#)
51. H. Mohan, M. B. Verhoog, K. K. Doreswamy, G. Eyal, R. Aardse, B. N. Lodder, N. A. Goriounova, B. Asamoah, A. B. Brakspear, C. Groot, S. van der Sluis, G. Testa-Silva, J. Obermayer, Z. S. Boudewijns, R. T. Narayanan, J. C. Baayen, I. Segev, H. D. Mansvelder, C. P. de Kock, Dendritic and axonal architecture of individual pyramidal neurons across layers of adult human neocortex. *Cereb. Cortex* **25**, 4839–4853 (2015). [doi:10.1093/cercor/bhv188](https://doi.org/10.1093/cercor/bhv188) [Medline](#)
52. R. Urbanczik, W. Senn, Learning by the dendritic prediction of somatic spiking. *Neuron* **81**, 521–528 (2014). [doi:10.1016/j.neuron.2013.11.030](https://doi.org/10.1016/j.neuron.2013.11.030) [Medline](#)
53. J. Hawkins, S. Ahmad, Why Neurons Have Thousands of Synapses, a Theory of Sequence Memory in Neocortex. *Front. Neural Circuits* **10**, 23 (2016). [doi:10.3389/fncir.2016.00023](https://doi.org/10.3389/fncir.2016.00023) [Medline](#)
54. L. T. Graybiel, T. L. Daigle, A. E. Sedeño-Cortés, M. Walker, B. Kalmbach, G. H. Lenz, E. Morin, T. N. Nguyen, E. Garren, J. L. Bendrick, T. K. Kim, T. Zhou, M. Mortrud, S. Yao, L. A. Siverts, R. Larsen, B. B. Gore, E. R. Szelenyi, C. Trader, P. Balam, C. T. J. van Velthoven, M. Chiang, J. K. Mich, N. Dee, J. Goldy, A. H. Cetin, K. Smith, S. W. Way, L. Esposito, Z. Yao, V. Gradinaru, S. M. Sunkin, E. Lein, B. P. Levi, J. T. Ting, H. Zeng, B. Tasic, Enhancer viruses for combinatorial cell-subclass-specific labeling. *Neuron* **109**, 1449–1464.e13 (2021). [doi:10.1016/j.neuron.2021.03.011](https://doi.org/10.1016/j.neuron.2021.03.011) [Medline](#)
55. C. J. Roome, B. Kuhn, Chronic cranial window with access port for repeated cellular manipulations, drug application, and electrophysiology. *Front. Cell. Neurosci.* **8**, 379 (2014). [doi:10.3389/fncel.2014.00379](https://doi.org/10.3389/fncel.2014.00379) [Medline](#)
56. M. Kabra, A. A. Robie, M. Rivera-Alba, S. Branson, K. Branson, JAABA: Interactive machine learning for automatic annotation of animal behavior. *Nat. Methods* **10**, 64–67 (2013). [doi:10.1038/nmeth.2281](https://doi.org/10.1038/nmeth.2281) [Medline](#)
57. A. Mathis, P. Mamidanna, K. M. Cury, T. Abe, V. N. Murthy, M. W. Mathis, M. Bethge, DeepLabCut: Markerless pose estimation of user-defined body parts with deep learning. *Nat. Neurosci.* **21**, 1281–1289 (2018). [doi:10.1038/s41593-018-0209-y](https://doi.org/10.1038/s41593-018-0209-y) [Medline](#)
58. J. Fienup, A. Kowalczyk, Phase retrieval for a complex-valued object by using a low-resolution image. *J. Opt. Soc. Am. A Opt. Image Sci. Vis.* **7**, 450 (1990). [doi:10.1364/JOSAA.7.000450](https://doi.org/10.1364/JOSAA.7.000450)

59. C. Stringer, M. Pachitariu, N. Steinmetz, M. Carandini, K. D. Harris, High-dimensional geometry of population responses in visual cortex. *Nature* **571**, 361–365 (2019). [doi:10.1038/s41586-019-1346-5](https://doi.org/10.1038/s41586-019-1346-5) [Medline](#)
60. M. T. Harnett, N. L. Xu, J. C. Magee, S. R. Williams, Potassium channels control the interaction between active dendritic integration compartments in layer 5 cortical pyramidal neurons. *Neuron* **79**, 516–529 (2013). [doi:10.1016/j.neuron.2013.06.005](https://doi.org/10.1016/j.neuron.2013.06.005) [Medline](#)